Petroleum Science 23 (2026) 5063–5080

Contents lists available at ScienceDirect

Petroleum Science

journal homepage: www.keaipublishing.com/en/journals/petroleum-science

Original Paper

Corrected model and charts for corrosion probe monitoring effectiveness in high-water-cut crude oil gathering pipelines with elevation changes

Min Qin [a,*], Xue-Ling Wu [a,**], Ke-Xi Liao [a], Long Qin [b], Guo-Xi He [a], Teng-Jiao He [a]

[a] Petroleum Engineering School, Southwest Petroleum University, Chengdu, 610500, Sichuan, China
[b] Sichuan Changning Natural Gas Development Co., Ltd., Yibin, 644005, Sichuan, China

ARTICLE INFO

Article history:
Received 10 September 2025
Received in revised form
20 November 2025
Accepted 21 January 2026
Available online 30 January 2026

Edited by Meng-Jiao Zhou

Keywords:
High-water-cut
Flow corrosion
Elevation changes
Electrical resistance probes
Monitoring effectiveness

ABSTRACT

Frequent corrosion perforation and monitoring effectiveness deviation have been observed in the undulating segments of high-water-cut crude oil gathering pipelines. This study proposes a corrected model and charts for in-pipe probe monitoring effectiveness (defined as the ratio of probe-measured corrosion rate to the circumferential maximum wall corrosion rate at the same cross-section). Computational fluid dynamics (CFD) simulations and loop experiments were conducted to systematically investigate the effects of flow velocity (0.4–1.2 m/s), temperature (20–60 °C), and monitoring time on probe effectiveness. The results show that monitoring effectiveness exhibits a "rise-then-fall" trend with increasing flow velocity, reaching 72.88% at 0.8 m/s and decreasing to 50.10% at 1.2 m/s. Elevated temperatures gradually reduce effectiveness, from 74.63% at 20 °C to 67.00% at 60 °C. With prolonged monitoring time, effectiveness significantly increases, rising from 5.15% at 12 h to 76.48% at 36 h. Based on these findings, a corrected corrosion rate model coupling velocity, temperature, and time was established, and charts illustrating corrected effectiveness under different conditions were generated. Field application indicates that the corrected probe monitoring effectiveness reaches 97.36% and 93.83% in the upward-inclined and downward-inclined segments, respectively, with an average improvement of 35.72%. The results provide effective technical support for corrosion monitoring and integrity management in complex undulating pipelines.

© 2026 The Authors. Publishing services by Elsevier B.V. on behalf of KeAi Communications Co. Ltd. This is an open access article under the CC BY-NC-ND license (http://creativecommons.org/licenses/by-nc-nd/4.0/).

1. Introduction

Pipelines are widely employed for large-scale transportation of oil and natural gas owing to their high safety, strong throughput capacity, and low operating cost (He et al., 2024). However, in the late stages of oilfield development, extensive water injection increases the water cut in gathering pipelines (Zhang et al., 2024). Under high water-cut conditions, corrosive species such as Cl^-, CO_2, and dissolved minerals markedly accelerate metal corrosion, resulting in wall thinning, perforation, and even failure, which poses serious threats to production safety and economic performance of stations (Hu et al., 2023; Wang et al., 2023; Zhao et al., 2024). Previous studies have shown that corrosion is particularly severe in undulating segments, and its sudden and irreversible nature makes corrosion prediction and monitoring critical for the safe operation of oil and gas fields. Therefore, the development of reliable corrosion monitoring and effectiveness correction methods holds significant engineering value and application potential.

Water is widely recognized as the primary driver of internal corrosion in oil and gas pipelines (Al-Moubaraki and Obot, 2021; Ma et al., 2023). As the water cut increases, the oil-water two-phase system gradually shifts to a water-continuous environment, thereby providing more favorable conditions for ion transport and electrochemical reactions (El Amine Ben Seghier et al., 2020; Yang et al., 2023c; Yu et al., 2022). Cl^- plays a particularly significant role by accelerating ion transport in the aqueous phase and compromising the integrity and stability of the corrosion product

* Corresponding author.
** Corresponding author.
E-mail addresses: 202499010132@swpu.edu.cn (M. Qin), wxl_a15@163.com (X.-L. Wu).

Peer review under the responsibility of China University of Petroleum (Beijing).

https://doi.org/10.1016/j.petsci.2026.01.039
1995-8226/© 2026 The Authors. Publishing services by Elsevier B.V. on behalf of KeAi Communications Co. Ltd. This is an open access article under the CC BY-NC-ND license (http://creativecommons.org/licenses/by-nc-nd/4.0/).

Nomenclature

a	Constant related to the exchange current density, dimensionless
A	Constant of flow velocity correction factor, dimensionless
b	Tafel slope, mV/decade
b_a	Anodic Tafel slope, mV/decade
b_c	Cathodic Tafel slope, mV/decade
B	Constant of flow velocity correction factor, dimensionless
c_p	Specific heat capacity, J/(kg·K)
C	Empirical constant, $C_{1\varepsilon} = 1.44$, $C_{2\varepsilon} = 1.92$, $C_{3\varepsilon} = 1.00$
d	Pipeline inner diameter, mm
De	Dean number, dimensionless
D	Mass diffusivity, m^2/s
E	Temperature correction constant, dimensionless
E_a	Activation energy of corrosion reaction, J/mol
F	Faraday constant, C/mol
$\vec{F}$	Applied body force, N/m^3
$\vec{g}$	Gravitational acceleration, m/s^2
G_k	Turbulent kinetic energy induced by velocity gradient, m^2/s^3
G_b	Turbulent kinetic energy induced by buoyancy, m^2/s^3
i	Current density, mA/cm^2
I	Unit tensor, dimensionless
i_{lim,H^+}	Cathodic limiting current density controlled by H^+ reduction, A/m^2
k	Turbulent kinetic energy, m^2/s^2
K_d	Mass transfer coefficient, m/s
L_i	Location of monitoring point, m (i = 1–180)
m	Pre-correction corrosion rate prediction coefficient
M	Post-correction corrosion rate prediction coefficient
n	Monitoring effectiveness correction coefficient, dimensionless
N	Number of electrons transferred, dimensionless
p	Static pressure, Pa
Q	Temperature correction constant, dimensionless
r	Pipeline radius, m
R	Universal gas constant, J/(mol·K)
R_c	Curvature radius of bend, m
Re	Reynolds number, dimensionless
Sc_{H^+}	Schmidt number of H^+, dimensionless
Sc	Schmidt number for ionic convective mass transfer, dimensionless
S_m	Mass added to continuous phase, g
t	Experimental time, h
T_0	Inlet temperature of pipeline medium, °C
T_i	Temperature, °C (i = 1–120)
T_{DL}	Corrected temperature, °C
T_{DU}	Temperature at the lower wall of the downward-inclined segment, °C
T_{UL}	Temperature at the lower wall of the upward-inclined segment, °C
T_{UU}	Temperature at the upper wall of the upward-inclined segment, °C
v	Inlet flow velocity, m/s
v_i	Fluid velocity, m/s (i = 1–180)
v_{corr}	Corrosion rate, mm/a
V_{DL}	Flow velocity at the internal probe of the downward-inclined segment, m/s
V_{DP}	Flow velocity at the internal probe of the downward-inclined segment, m/s
V_{DU}	Flow velocity at the upper wall of the downward-inclined segment, m/s
V_{UL}	Flow velocity at the lower wall of the upward-inclined segment, m/s
V_{UP}	Flow velocity at the internal probe of the upward-inclined segment, m/s
V_{UU}	Flow velocity at the upper wall of the upward-inclined segment, m/s
x_i, x_j	Spatial coordinates
Y_M	Contribution of fluctuating diffusion in compressible turbulence, W/m^3
α_a	Anodic charge-transfer coefficient, dimensionless
α_c	Cathodic charge-transfer coefficient, dimensionless
ε	Turbulent dissipation rate, W/m^3
η	Overpotential, mV
λ	Thermal conductivity, W/(m·K)
μ	Dynamic viscosity, Pa·s
μ_t	Turbulent viscosity, Pa·s
υ	Kinematic viscosity, m^2/s
σ_k	Turbulent Prandtl number for k-equation
σ_ε	Turbulent Prandtl number for ε-equation
ρ	Density, kg/m^3
τ	Wall shear stress, Pa
∇	Nabla operator

film, thereby promoting pitting corrosion (Ma et al., 2024; Zeng et al., 2020, 2021). The effect of cathodic reactions, such as hydrogen ion reduction, on corrosion-enhanced erosion (C-E) has been studied in various environments, showing significant impacts under high-water-cut and complex flow conditions (Zhang et al., 2025). Researchers used the OLGA multiphase flow simulation software and ANSYS Fluent to model the liquid holdup and liquid accumulation in wet gas pipelines, thereby further identifying corrosion-prone pipeline segments (Liao et al., 2021; Qin et al., 2023). Temperature and flow velocity also significantly affect corrosion characteristics (Krishnan et al., 2023; Peng et al., 2024). At low temperatures (303–393 K), $FeCO_3$ crystals in the corrosion product film are dense and relatively stable, providing some substrate protection (Li et al., 2020; Sun et al., 2023). Meanwhile, flow velocity variations directly affect interfacial shear stress and mass transfer capability. Under high flow velocity conditions, the corrosion product film is more easily eroded, accelerating localized corrosion (Atashin et al., 2013; Zhao et al., 2022). Additionally, cathodic reactions can synergistically amplify erosion-corrosion in sand-entraining electrolytes, shifting between uniform and pitting damage modes (Fan et al., 2025). In actual gathering systems, temperature, mixture velocity, and water cut are strongly coupled through flow-pattern transitions, liquid holdup, and wettability dynamics-further intertwined with thermal/compositional effects-rather than acting independently. This coupling has been demonstrated in inclined pipes, where velocity and inclination jointly drive stratified-to-slug transitions (altering holdup and near-wall shear) (Abdul-Majeed et al., 2024), and in wellbore/pipe systems under high gas-to-liquid ratios, where flow and phase behavior co-evolve (Hong et al., 2025).

Various data-driven and intelligent algorithm-based methods have been proposed for corrosion prediction (Ben Seghier et al., 2022; Wang et al., 2024). These methods generally rely on monitoring data for model training and are then used to forecast the

dynamic evolution of corrosion. Du et al. (2023) developed a pitting depth prediction model using automated machine learning (AML), which primarily focuses on static assessment, heavily depends on historical data, and struggles to reflect the complex dynamics of corrosion (Cao et al., 2023; Wasim and Djukic, 2022). Other approaches, such as multivariate adaptive regression splines (MARS), random forests, and gradient-boosted regression trees, have also been explored to link corrosion prediction with systemic factors for assessing corrosion risk in crude oil pipelines (Ben Seghier et al., 2022; Przybyłek et al., 2019). However, existing prediction studies generally do not fully account for the non-uniform corrosion distribution caused by the complex flow fields in undulating pipelines or the bias in monitoring data, thereby limiting the reliability of predictions in actual high-water-cut crude oil gathering pipeline segments.

In fact, variations in the geometric inclination of undulating pipelines induce pronounced flow non-uniformity. This non-uniform flow not only modifies local corrosion mechanisms but also causes measurements based on local probes or uniform flow assumptions to deviate from actual corrosion conditions, thereby affecting prediction accuracy. Consequently, real-time corrosion-monitoring methods have attracted increasing attention. Intrusive methods remain the mainstay for internal corrosion monitoring in pipelines, including weight-loss coupons, electrical-resistance (ER) probes, and linear-polarization-resistance (LPR) probes, and these are supplemented by non-intrusive techniques such as ultrasonic testing (UT) wall-thickness surveys and in-line inspection (ILI) (Shin et al., 2022; Soleymani, 2023). Recent research has also advanced sensor technologies. Wire-beam electrode (WBE) sensors can reveal spatial corrosion distributions and improve reproducibility through structural optimization (He et al., 2023; Laleh et al., 2023; Liu et al., 2021; Yang et al., 2024). Piezoelectric active sensing combined with time-reversal allows real-time monitoring of inner-wall corrosion by analyzing ultrasonic-signal attenuation (Yang et al., 2023). Distributed fiber-optic sensing and methods combining wavelet-packet energy with convolutional neural networks (WPE-CNN) can quantify and visualize corrosion online (Tan et al., 2021; Yang et al., 2023b). In particular, integrated EC-SPR fiber sensors enable in-situ nanoscale tracking of passive-film growth under high-salinity conditions (Wang et al., 2025).

Although the above monitoring techniques perform well in laboratory or small-scale pipeline tests, their sensitivity, representativeness, and engineering applicability remain limited under the complex flow fields of field-scale undulating pipelines. In contrast, resistance probes are widely used on-site in oilfields due to their low cost, ease of deployment, and ability to provide continuous measurements. However, in undulating pipelines, local turbulence, liquid scouring, and flow non-uniformity often cause probe measurements to deviate from actual pipe wall corrosion. This underscores the need for a probe-based monitoring effectiveness correction model to enable reliable corrosion assessment under complex flow conditions. Accordingly, this study focuses on high-water-cut crude oil gathering undulating pipelines, integrating numerical simulations with experimental investigations to propose a probe effectiveness correction method and generate corresponding charts. The approach provides a practical engineering solution for online corrosion monitoring in oilfields, enhancing monitoring accuracy and protection of gathering pipelines.

2. Methodology

2.1. Theoretical model

The theoretical calculation model for high-water-cut crude oil gathering undulating pipelines includes the mass conservation equation, momentum conservation equation, and energy conservation equation.

1) The mass conservation equation describes the relationship between the temporal change of mass in a unit fluid volume and the fluid velocity, as given in Eq. (1).

$$\frac{\partial \rho}{\partial t} + \nabla \cdot (\rho \vec{v}) = S_{\mathrm{m}} \tag{1}$$

For incompressible fluids, the mass conservation equation can be simplified as Eq. (2).

$$\nabla \cdot (\rho \vec{v}) = S_{\mathrm{m}} \tag{2}$$

2) The momentum conservation equation describes the relationship between the temporal change of momentum in the fluid and the forces acting upon it. It is used to predict fluid velocity, flow behavior, and force distribution, as expressed in Eq. (3).

$$\frac{\partial \rho}{\partial t}(\rho \vec{v}) + \nabla \cdot (\rho \vec{v}\vec{v}) = -\nabla p + \nabla \cdot \left\{ \mu \left[(\nabla \vec{v} + \nabla \vec{v}^{T}) - \frac{2}{3} \nabla \cdot \vec{v} I \right] \right\} + \rho \vec{g} + \vec{F} \tag{3}$$

3) The energy conservation equation describes the relationship between the rate of change of total energy per unit mass and the heat transfer and work performed on the fluid. Solving this equation allows determination of the fluid temperature distribution and heat transfer, enabling simulation and prediction of energy conversion, as expressed in Eq. (4).

$$\frac{\partial (\rho T)}{\partial t} + \nabla \cdot (\rho u T) = \nabla \cdot \left(\frac{k}{c_{\mathrm{p}}} \nabla T \right) + S_{\mathrm{h}} \tag{4}$$

Under the simulated pipe flow conditions, the Reynolds number exceeds 2300, indicating fully turbulent flow within the pipe. Accordingly, a turbulence model is employed. Turbulence models based on the Reynolds-averaged Navier-Stokes (RANS) equations describe the interaction between the mean flow and turbulent fluctuations by averaging vortical motions. The realizable k–ε model, capable of accurately capturing jet diffusion and flow development, is thus selected for simulating jet dispersion, with its governing equations provided in Eqs. (5) and (6).

$$\frac{\partial (\rho k)}{\partial t} + \frac{\partial (\rho v_i k)}{\partial x_i} = G_{\mathrm{k}} + G_{\mathrm{b}} - \rho \varepsilon - Y_{\mathrm{M}} + \frac{\partial \left[\left(\mu + \frac{\mu_t}{\sigma_k} \right) \frac{\partial k}{\partial x_j} \right]}{\partial x_j} \tag{5}$$

$$\frac{\partial (\rho \varepsilon)}{\partial \tau} + \frac{\partial (\rho \mu_i \varepsilon)}{\partial x_i} = C_{1\varepsilon} \frac{\varepsilon}{k} (G_{\mathrm{k}} + C_{3\varepsilon} G_{\mathrm{b}}) p_t - C_{2\varepsilon} \rho \frac{\varepsilon^2}{k} + \frac{\partial \left[\left(\mu + \frac{\mu_t}{\sigma_\varepsilon} \right) \frac{\partial \varepsilon}{\partial x_j} \right]}{\partial x_j} \tag{6}$$

A correction model and method for corrosion probe monitoring effectiveness in high-water-cut crude oil gathering pipelines with elevation changes are proposed. The flowchart is shown in Fig. 1.

2.2. Geometric modeling

The undulating liquid pipeline model was constructed with inclination angles of 45° and −45°. Each inclined segment is 500 mm long, with pipe dimensions of φ 108 × 4 mm and a bend radius of 216 mm. For clarity in analyzing the simulation results, segments

were designated along the upward-inclined and downward-inclined pipe segments. In the upward-inclined segment, sections from bottom to top are labeled S1 to S6, while in the downward-inclined segment, sections from top to bottom are labeled X6 to X1. Positions across each pipe cross-section include the upper wall, lower wall, and section center. A schematic is presented in Fig. 2.

2.3. Parameter settings

Turbulence models are commonly formulated on the basis of the Reynolds-averaged Navier-Stokes (RANS) equations. The eddy motions in turbulent flow are averaged to capture the interaction between the mean flow field and the turbulent fluctuations. Representative models are the Spalart-Allmaras model, the k–ω model, the SST k–ω model, the Reynolds stress model (RSM), and large-eddy simulation (LES). In CFD practice, the k–ε family is most commonly employed. Three variants are widely used: the Standard k–ε model, the RNG k–ε model, and the realizable k–ε model. The characteristics of these models are summarized in Table 1.

This paper adopts the realizable k–ε model as the turbulence model because it satisfies realizability (normal-stress) constraints and improves stress closure for rotating and curved shear layers as well as free-shear development relative to the Standard and RNG k–ε models. These features are pertinent to secondary flows induced by elbows and inclination. Near-wall effects were treated using the Enhanced Wall Treatment. Pressure-velocity coupling was applied, and the momentum, turbulent kinetic energy, and turbulence dissipation terms were discretized using a second-order upwind scheme. The convergence criterion was set to 1×10^{-6}.

2.4. Boundary conditions

Boundary conditions were defined with a velocity inlet and a pressure outlet, and walls were treated as heat-exchanging surfaces at an ambient temperature of 20 °C. Under steady-state operation, the target gathering pipeline typically runs at 0.4–1.2 m/s and 20–60 °C, with occasional conditions approaching the upper bounds. The flow is fully turbulent across 20–60 °C. Accordingly, the inlet velocities for the simulation cases were 0.4, 0.6, 0.8, 1.0, and 1.2 m/s, and the fluid temperatures were 20, 30, 40, 50, and 60 °C. A total of eleven simulation cases were conducted, as summarized in Table 2.

2.5. Mesh generation

The undulating liquid pipeline model employed a structured hexahedral mesh with boundary-layer refinement near the pipe walls to achieve a first-layer (y^+) of approximately 1, as shown in Fig. 3. Based on the number of elements, three mesh schemes with different levels of resolution were established.

2.6. Experimental specimens and solutions

Both the pipeline and the probe materials were from the same batch of 20# steel. The principal elements were Fe, C, Si, and Mn;

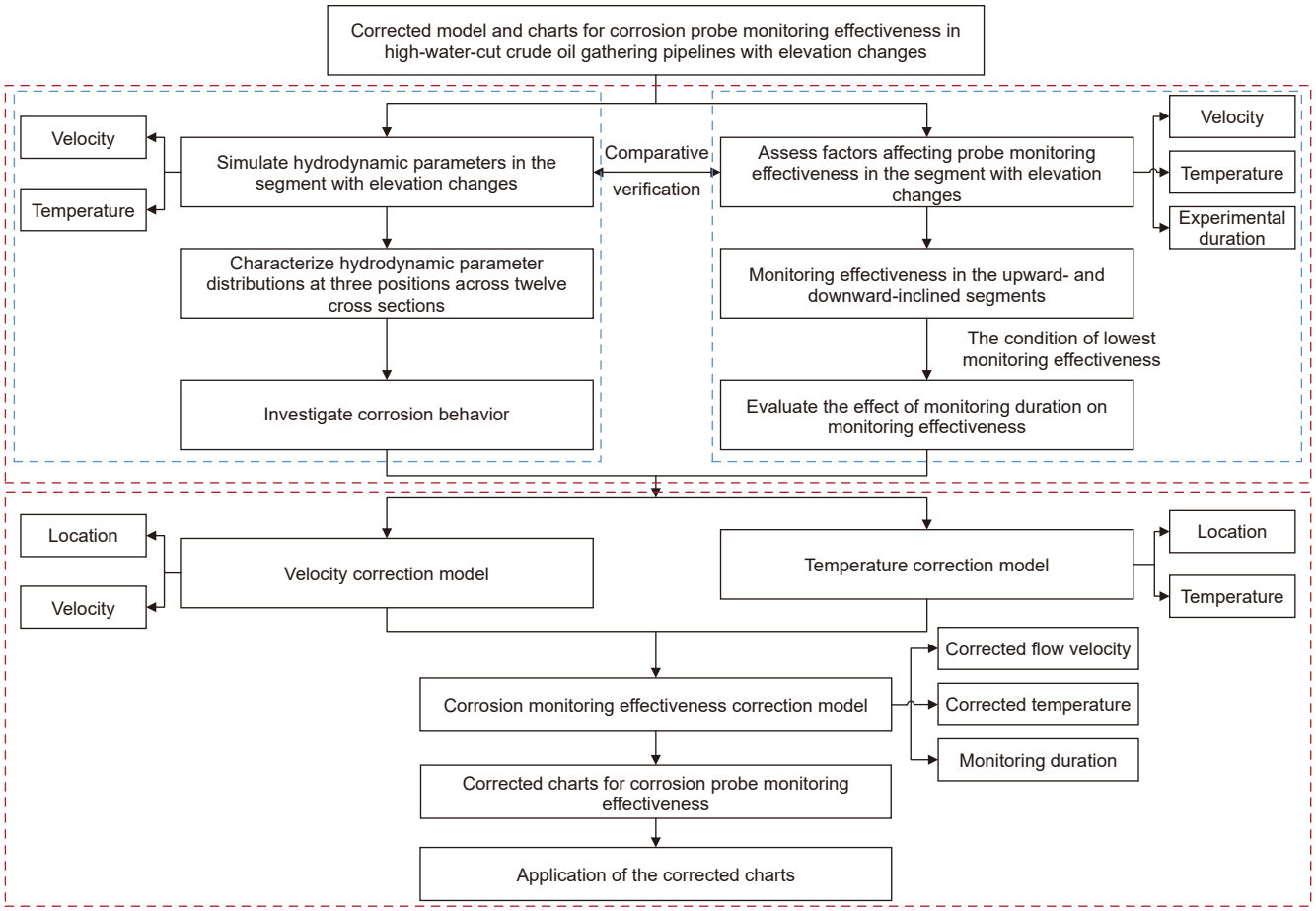


Fig. 1. Flowchart of the correction method for corrosion probe monitoring effectiveness.

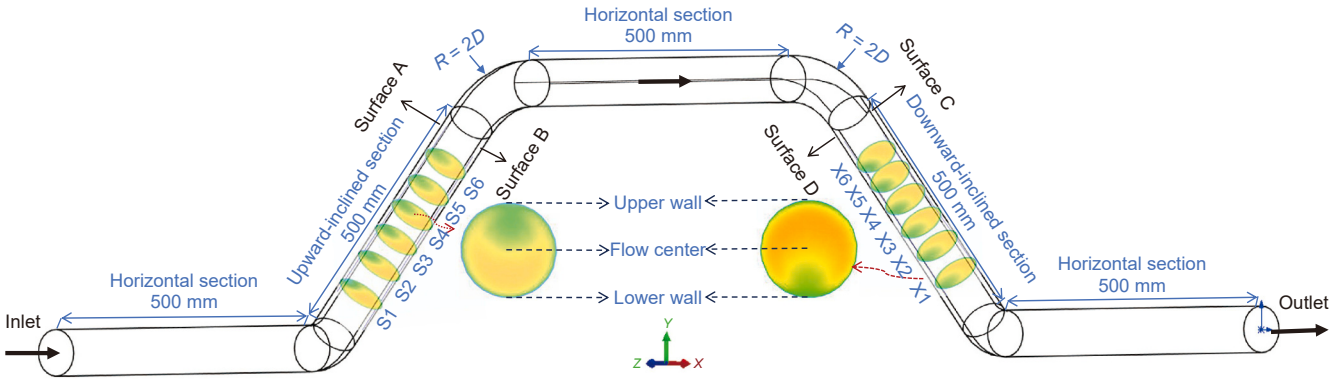


Fig. 2. Model of the undulating liquid pipeline.

Table 1
Characteristics of k–ε turbulence models.

Model	Turbulent viscosity	Basic characteristics	Application conditions
Standard k–ε model	Neglects the influence of molecular viscosity	Only effective for high Reynolds number turbulence	More data accumulation and higher accuracy
RNG k–ε model	Vortex corrected turbulent viscosity	Improve the ε equation, suitable for moderate-intensity swirl and low-Reynolds-number flow	Simulates moderately complex flows
Realizable k–ε model	Adds turbulent viscosity calculation formula	Suitable for predicting moderate intensity vortices	Reasonable accuracy for circular/planar jets

Table 2
Simulation conditions.

Case number	Velocity, m/s	Temperature, °C
1	0.4	40
2	0.6	40
3	0.8	20
4		30
5		40
6		50
7		60
8	1.0	40
9	1.2	40
10		
11		

the detailed composition is given in Table 3. In the flow-loop experiments, the electrode had a working surface diameter of 16 mm and a height of 100 mm. Prior to installation, the working surface of the electrode was sequentially ground with 400-, 800-, 1000-, and 1200-grit silicon carbide sandpaper, followed by polishing using a polishing machine. After polishing, any residues on the electrode surface were removed using deionized water and absolute ethanol in an ultrasonic cleaner. The specimens were then air-dried before use. The experimental solution was a 50000 mg/L NaCl solution. Deoxygenation and CO_2 sparging were performed at ambient temperature (25 ± 1 °C). At this temperature, N_2 purging was applied for 2 h to reduce dissolved oxygen (DO) to <0.5 mg/L. CO_2 was then bubbled into the solution for ≥12 h until saturation was reached. The temperature was adjusted to the experimental setpoint (20, 30, 40, 50, or 60 °C). The water temperature was maintained within ±1 °C of the setpoint.

2.7. Experimental setup and procedure

The experimental loop is shown in Fig. 4. The test section reproduces an undulating high-water-cut crude oil gathering pipeline, with upward-inclined and downward-inclined segments at angles of 45° and −45°, each 500 mm in length. The test section pipe has a specification of 108 × 4 mm. The overall loop system consists of a storage tank, a centrifugal pump, pressure gauges, the upward-inclined and downward-inclined test segments, an electrochemical workstation, N_2 and CO_2 cylinders, an electromagnetic flowmeter, and a controller. Monitoring points were set on the downward-inclined segment and on the upward-inclined segment of the undulating section. They were located approximately 0.40 m from the elbow apex along the flow direction. On the upward-inclined segment, the probe was installed at the pipe top. On the downward-inclined segment, the probe was installed at the pipe bottom. The probe was positioned at the pipe wall with its axis oriented normal to the inner wall. Electrical isolation was adopted between the probe housing and the sensing element/pipe body. The placement of the monitoring point 0.40 m from the

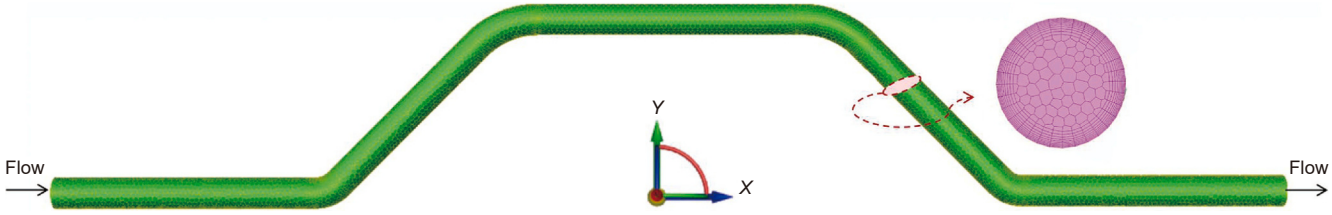


Fig. 3. Mesh of the undulating liquid pipeline generated.

Table 3
Elemental composition of 20# steel.

Element	Fe	C	Si	Mn	P	S	Ni	Cr	Cu
Content, wt%	≥98	0.17–0.23	0.17–0.37	0.35–0.65	≤0.035	≤0.035	≤0.03	≤0.25	≤0.25

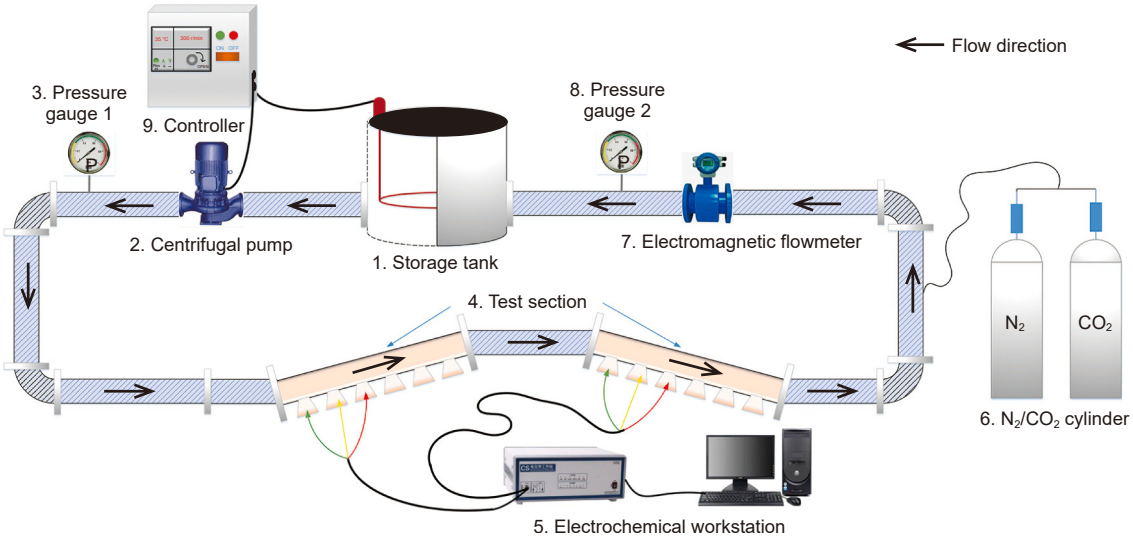


Fig. 4. Schematic diagram of the flow corrosion experimental loop.

elbow was determined on the basis of flow-field simulations to ensure that the point lies in a fully developed flow region and is subject to minimal elbow-induced disturbance. CFD results show that elbow-induced secondary flow decays progressively over a downstream axial distance. At 0.40 m from the elbow, the near-wall shear stress and the velocity profile have stabilized at representative levels. The direct disturbance from the elbow has largely dissipated, avoiding reading bias caused by strong shear and recirculation near the elbow. The upward-inclined segment and the downward-inclined segment use the same axial offset (0.40 m) and a fixed circumferential position and orientation. This design enables like-for-like comparisons and statistical analysis across operating conditions.

During the experiments, positions S6 and X6 were selected as monitoring points in the turbulence core regions. The inlet velocity of the test section was adjusted by varying the speed of the loop pump, while the fluid temperature was controlled via the control unit to meet the requirements of different experimental conditions. Electrochemical measurements were performed using a CS301H electrochemical workstation, including Electrochemical Impedance Spectroscopy (EIS) and Polarization Curve measurements. The electrochemical experiments were based on a three-electrode system, consisting of a Reference Electrode (RE), a Counter Electrode (CE), and a Working Electrode (WE). Both the RE and CE were installed on the pipe wall of the test section, whereas the WE was the electrochemical probe placed at the center of the pipe. After stabilization of the open circuit potential (OCP) of the carbon steel working electrode, EIS measurements were conducted over a frequency range of 10^5 Hz to 10^{-2} Hz. Polarization curves were measured at a scan rate of 1 mV/s, from the cathodic to the anodic region, with a potential range of OCP ±5 mV. Each experiment was repeated three times to ensure data reproducibility and reliability.

Due to the large number of monitoring points, each point was labeled for clarity, as shown in Fig. 5. Four working electrode measurement points were distributed on the pipe wall, labeled A, B, C, and D along the flow direction on the upper and lower walls, while the probes were labeled T1 and T2. Specifically, point A represents the monitoring point on the upper wall of the upward-inclined segment, point B represents the lower wall monitoring point of the upward-inclined segment, and T1 represents the internal probe monitoring point of the upward-inclined segment. Similarly, point C represents the upper wall monitoring point of the downward-inclined segment, point D represents the lower wall monitoring point of the downward-inclined segment, and T2 represents the internal probe monitoring point of the downward-inclined segment.

2.8. Experimental conditions

A total of 11 experimental runs with different combinations of flow velocity and temperature were designed, maintaining

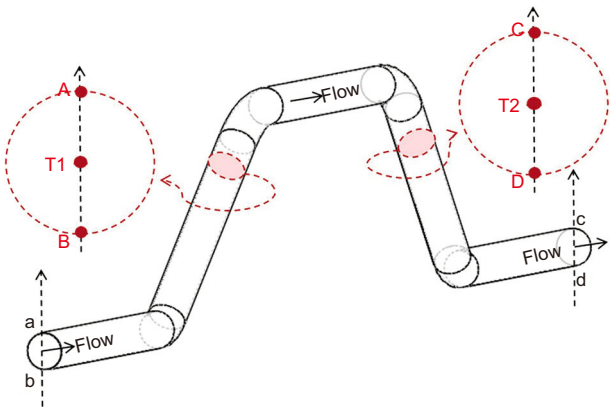


Fig. 5. Schematic diagram of the monitoring point labels in the test section.

consistency with the CFD simulations (Table 2). Each experiment lasted 36 h, aiming to systematically evaluate the monitoring effectiveness of corrosion probes under high-water-cut crude oil gathering conditions. By comparing probe monitoring results under all conditions, the condition with the lowest monitoring effectiveness (flow velocity 1.2 m/s, temperature 40 °C) was selected as the typical case for further study. For this typical condition, three experimental durations (12, 24, and 36 h) were set to investigate the influence of monitoring time on the corrosion probe effectiveness. A flow velocity of 1.2 m/s was selected because it lies at the upper endpoint of the study's velocity range (0.4–1.2 m/s). This choice markedly increases near-wall shear and the intensity of curvature-induced secondary flow, which helps amplify and identify monitoring deviations. 40 °C lies near the center of the experimental temperature matrix. The electrochemical state is more stable and the spectra are smoother, which facilitates EIS and polarization fitting and time-series comparisons (12/24/36 h). In the experimental loop, this operating condition exhibited good temporal stationarity and a high signal-to-noise ratio, enabling replicate experiments. The correction model and parameter regressions were developed from the complete dataset (0.4–1.2 m/s; 20–60 °C; multiple locations and durations). The typical condition is used only for illustration and mechanism explanation and does not affect the generality of the conclusions.

3. Results

3.1. Model validation

Under a fluid velocity of 1.5 m/s, velocity measurements were conducted at the upward-inclined pipe segment at the position (0.05, −0.09, 0) to obtain the velocity distribution under different mesh densities. Grid independence was verified using three mesh schemes with 965467, 998948, and 1016754 elements, respectively. As shown in Fig. 6, the results of the medium- and high-density meshes were in excellent agreement, whereas the low-density mesh produced significantly different velocities. Considering both computational accuracy and resource consumption, the medium-density mesh scheme (998948 elements) was selected for subsequent numerical simulations.

CFD predictions were compared with experimental measurements to validate the model. A thermometer was installed at the elbow on the downward-inclined segment. As shown in Fig. 7(a), the mean absolute error between computed and measured temperatures was 1.2%. The bias at higher temperatures is mainly attributed to modeling the pipe wall as a convective boundary to an ambient of 20 °C and neglecting solid-fluid conjugate heat transfer and radiation. Flow velocity was validated by comparing the CFD-predicted velocity with the average velocity converted from the field flowmeter's volumetric flow rate. As shown in Fig. 7(b), the mean absolute error was 2%. The deviation at low velocities arises primarily because the CFD cross-sectional average uses only the normal velocity component and does not include the tangential component of the secondary flow. Differences in the treatment of inlet and local minor losses also contribute. The mean absolute errors for temperature and velocity are both below 5%. The accuracy is therefore acceptable for engineering purposes and suitable for analyzing corrosion-monitoring effectiveness in high-water-cut crude oil gathering pipelines with elevation changes.

3.2. Three-dimensional velocity distribution

Fig. 8 presents the axial and cross-sectional velocity distributions of the upward-inclined and downward-inclined segments under different inlet velocities. The center velocity is consistently higher than that near the walls. In the upward-inclined segment, the distribution follows $v_{center} > v_{lower\ wall} > v_{upper\ wall}$, while in the downward-inclined segment it follows $v_{center} > v_{upper\ wall} > v_{lower\ wall}$. Along the flow direction, velocities at the center and lower wall of the upward-inclined segment decrease, whereas the upper wall velocity slightly increases; in the downward-inclined segment, the center and upper wall velocities decrease, while the lower wall velocity rises. These trends, governed by gravity and wall shear, cause fluid to shift toward the lower side in the upward-inclined segment and the upper side in the downward-inclined segment, bringing the center velocity closer to the inclined wall. The maximum velocity occurs at the center of section X6, and the minimum at the upper wall of section S1, reflecting the velocity field evolution under axial flow and cross-sectional non-uniformity.

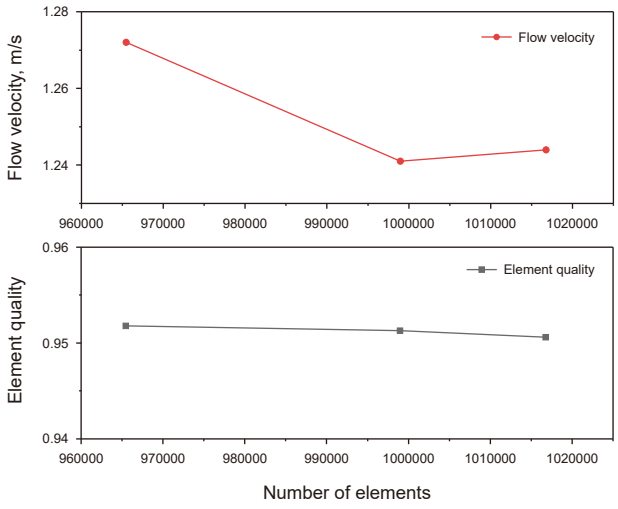


Fig. 6. Grid independence verification. **(a)** Flow velocity, **(b)** element quality.

Fig. 9 presents velocity distributions at different cross-sectional positions. With increasing inlet velocity, the difference between the center and wall velocities enlarges. At 0.4 m/s, the maximum and minimum velocities occur at the section center (0.47 m/s) and upper wall (0.18 m/s), with a center-lower wall difference of 0.29 m/s. At 1.2 m/s, the same locations exhibit velocities of 1.37 m/s and 0.62 m/s, and the difference increases to 0.75 m/s. This growing disparity alters the energy and flow fields, producing marked differences in corrosion between the wall and fluid core, thereby reducing probe monitoring effectiveness.

Due to pipeline inclination, the entering fluid forms a “core vortex” which develops into a Dean vortex under viscous and centrifugal forces. The Dean number, indicating vortex strength, increases with secondary flow intensity (Zhou et al., 2025). Two counter-rotating, non-uniform vortices appear in all cross-sections, shifting downward in the upward-inclined segment and upward in the downward-inclined segment. Their distribution is governed by vortex intensity. Under fully turbulent conditions, resistance is proportional to velocity squared, as shown in Eq. (7), so higher velocity enhances recirculation and separation.

$$De = Re \cdot (r/R_c)^{0.5} = u \cdot 2r \cdot \upsilon^{-1} \cdot (r/R_c)^{0.5} \quad (7)$$

Changes in inlet velocity alter the Dean number and consequently the secondary flow structures. With increasing Dean number, enhanced secondary flows intensify mass transfer and modify radial velocity distribution, leading to larger concentration gradients of corrosion products along the pipe wall. This not only

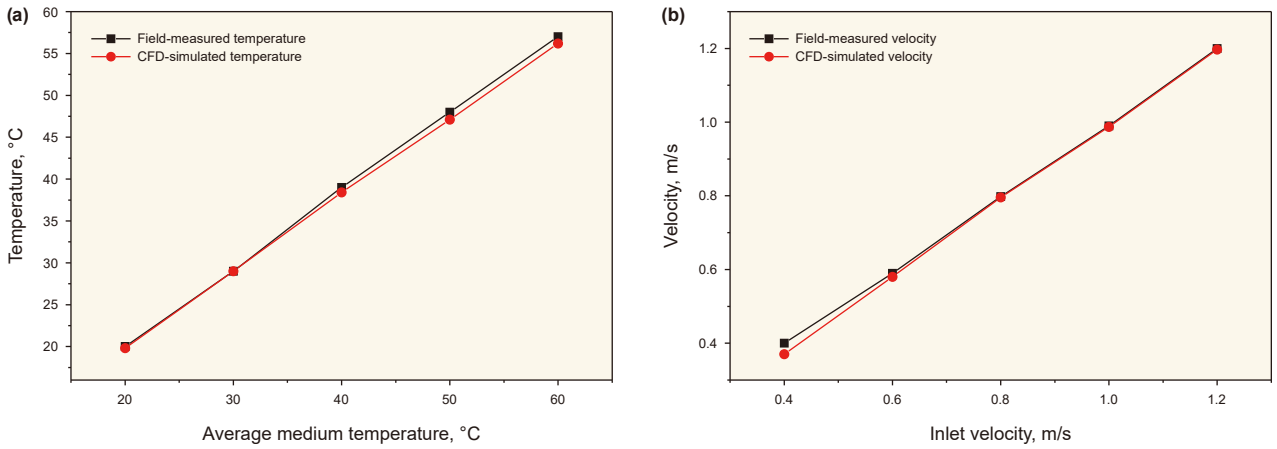


Fig. 7. Comparison between CFD-simulated and field-measured. **(a)** Temperature, **(b)** velocity.

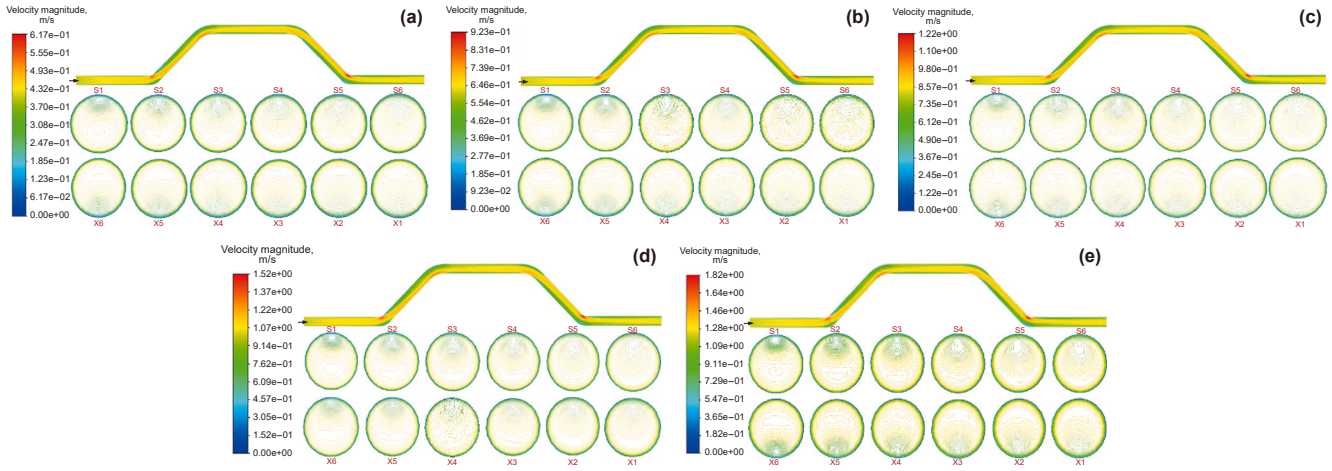


Fig. 8. Cross-sectional velocity distributions along the flow direction at different inlet velocities. **(a)** $v = 0.4$ m/s, **(b)** $v = 0.6$ m/s, **(c)** $v = 0.8$ m/s, **(d)** $v = 1.0$ m/s, **(e)** $v = 1.2$ m/s.

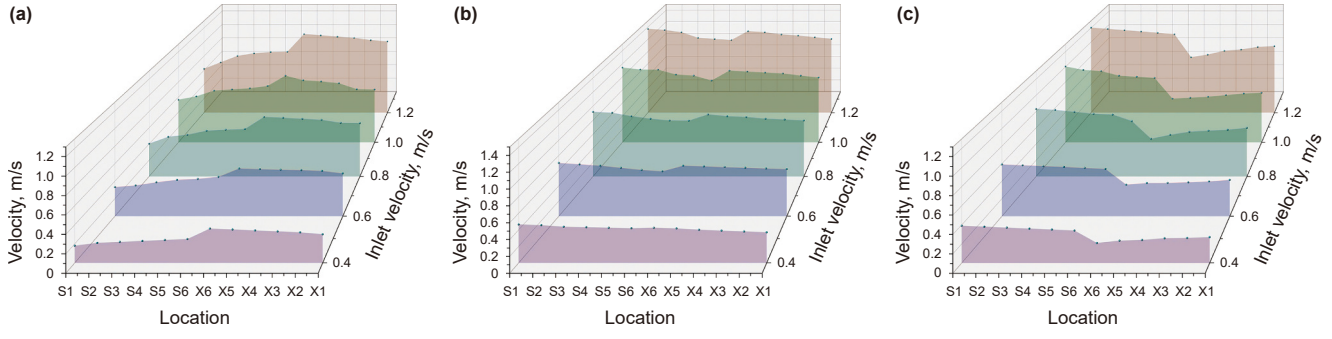


Fig. 9. Velocity at different positions within the cross-section. **(a)** Upper wall, **(b)** section center, **(c)** lower wall.

elevates the overall corrosion rate but also amplifies spatial differences in corrosion severity.

3.3. Shear stress distribution

Fig. 10 presents shear stress contours of the upward-inclined and downward-inclined segments at different inlet velocities. A distinct non-uniform distribution is observed, with $F_D > F_B > F_A > F_C$. Surface D shows the highest value (2.80 Pa), while surface A is the lowest (1.5 Pa). In the upward segment, shear stress on surface B is 1.72 times that of A, whereas in the downward segment, surface D is 1.86 times that of C. These differences arise from lateral deviation and gravity effects, producing asymmetric wall velocity profiles and localized stress peaks. With increasing velocity, enhanced inertia enlarges near-wall gradients, raising overall shear stress.

The average wall shear stress at different surfaces under varying inlet velocities is shown in Fig. 11. At 0.4 m/s, the mean value is 0.56 Pa, with Surface B exceeding A by 0.4 Pa and surface D

exceeding C by 0.41 Pa. At 1.2 m/s, the average rises to 4.00 Pa, with B 1.51 times A and D 1.72 times C. At low velocities, shear stress is controlled by viscosity and gradual film formation, yielding minor surface differences. At higher velocities, inertial effects dominate, velocity gradients intensify, and inclination drives fluid toward one wall, producing asymmetric stress peaks. Wall shear stress is thus highly velocity-sensitive and increases nonlinearly.

3.4. Turbulent kinetic energy distribution

Fig. 12 shows the turbulent kinetic energy (TKE) distribution across sections at different inlet velocities. High TKE appears near the upper wall in the upward-inclined segment and near the lower wall in the downward-inclined segment, while the section center consistently exhibits the lowest values. The distributions follow $TKE_{lower\ wall} > TKE_{upper\ wall} > TKE_{center}$ in the upward segment and $TKE_{upper\ wall} > TKE_{lower\ wall} > TKE_{center}$ in the downward segment. The maximum TKE occurs at the upper wall of section X1, and the minimum at the center of section S1. With increasing velocity, turbulence intensity rises and wall-center differences enlarge, as inclination drives fluid shifting, steepens velocity gradients, and concentrates energy near the walls, whereas the center remains less affected by shear and inertia.

Fig. 13 presents the TKE at different cross-sectional positions. At an inlet velocity of 0.4 m/s, the average TKE is 0.0018 m^2/s^2, with minimal wall-center differences. The maximum occurs at the upper wall of section X1 (0.0040 m^2/s^2) and the minimum at the center of section S1 (0.0010 m^2/s^2), where the upper and lower wall values are 2.24 and 1.28 times that of the center, respectively. When the inlet velocity increases to 1.2 m/s, the average TKE rises to 0.0152 m^2/s^2, 8.44 times that at 0.4 m/s. Although the locations of extrema remain unchanged, wall-center differences grow markedly, with the upper-wall TKE reaching 3.81 times and the lower-wall TKE 3.21 times that of the section center, due to dual vortices enhancing velocity gradients and intensifying near-wall turbulence.

3.5. Temperature distribution

Fig. 14 shows the temperature distribution at different cross-sectional positions. Due to heat exchange with the environment, wall temperatures are consistently lower than those at the section center. In the upward-inclined segment, the lower wall exhibits a higher temperature than the upper wall, whereas in the downward-inclined segment, the reverse occurs. As temperature

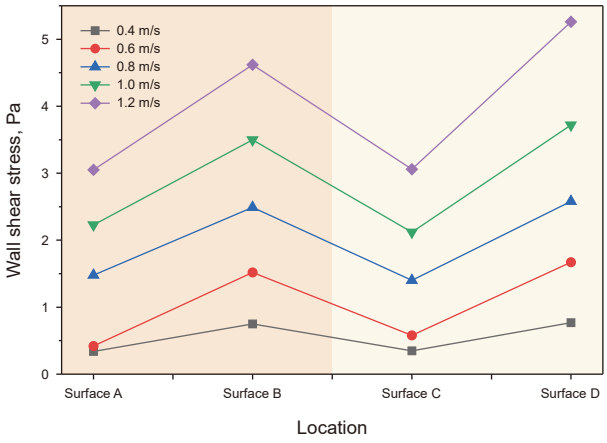


Fig. 11. Average wall shear stress at different surfaces under varying inlet velocities.

rises, both inter-sectional and wall-center temperature differences increase. At 20 °C, the differences are minimal; at 30 °C, the maximum differences reach 1.69 °C (upward-inclined segment) and 1.90 °C (downward-inclined segment). At 60 °C, wall-center differences increase to 5.6 °C and 6.0 °C, respectively. These gradients influence the base metal corrosion rate and the compactness of corrosion product films, leading to significant discrepancies in corrosion behavior between the pipe wall and the probe surface, thereby reducing monitoring effectiveness.

3.6. Mass transfer coefficient

The dimensionless Schmidt number (Sc) was used to correlate mass transfer with flow, and since the mass transfer coefficient is closely related to wall shear stress, the coefficient K_d was calculated using Eqs. (8) and (9).

$$Sc = \frac{\upsilon}{D} \tag{8}$$

$$K_d = 17.24\left(\frac{\tau}{\rho}\right)^{\frac{1}{2}} Sc^{\frac{2}{3}}, Sc > 100 \tag{9}$$

Fig. 15 presents the mass transfer coefficients at different locations, ranging from 5×10^{-5} to 3.2×10^{-4} m^2/s. The maximum occurs at the center of section S1, while the minimum is at the

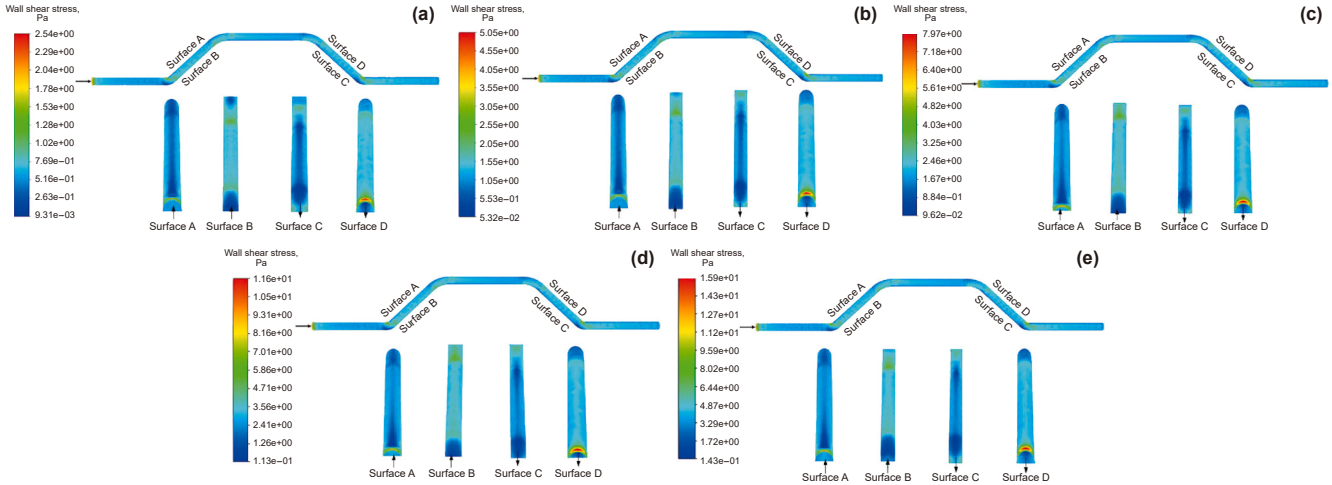


Fig. 10. Wall shear stress distribution of the pipeline at different inlet velocities. **(a)** $v = 0.4$ m/s, **(b)** $v = 0.6$ m/s, **(c)** $v = 0.8$ m/s, **(d)** $v = 1.0$ m/s, **(e)** $v = 1.2$ m/s.

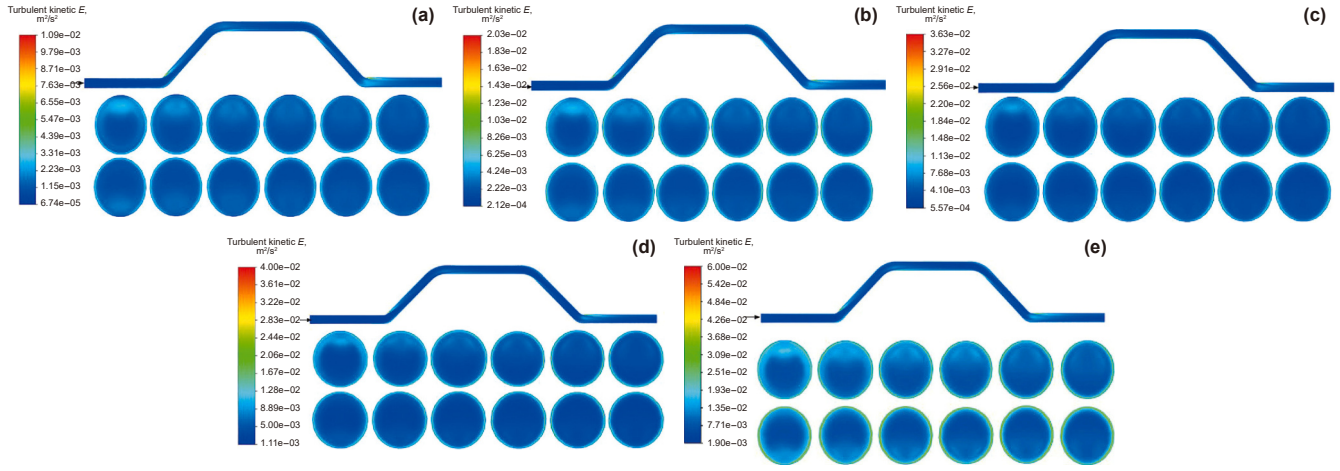


Fig. 12. Contours of turbulent kinetic energy (TKE) across pipeline sections at different inlet velocities. **(a)** $v = 0.4$ m/s, **(b)** $v = 0.6$ m/s, **(c)** $v = 0.8$ m/s, **(d)** $v = 1.0$ m/s, **(e)** $v = 1.2$ m/s.

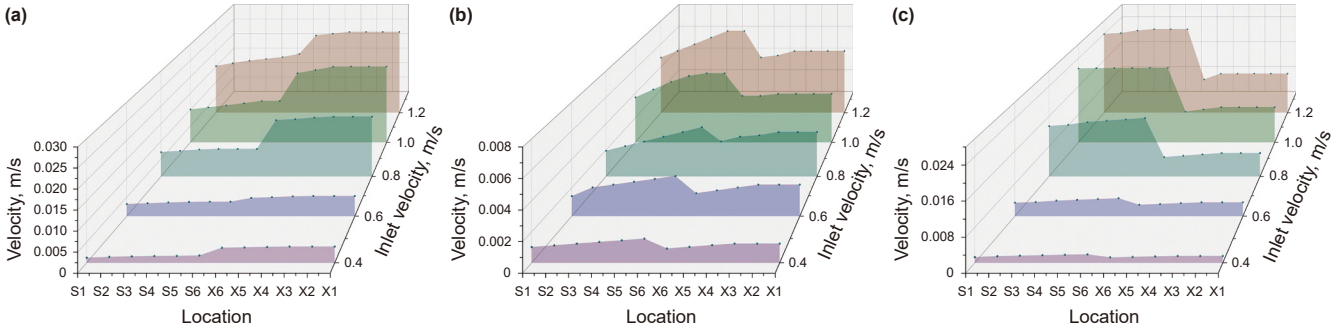


Fig. 13. Turbulent kinetic energy (TKE) at different positions across the section. **(a)** Upper wall, **(b)** section center, **(c)** lower wall.

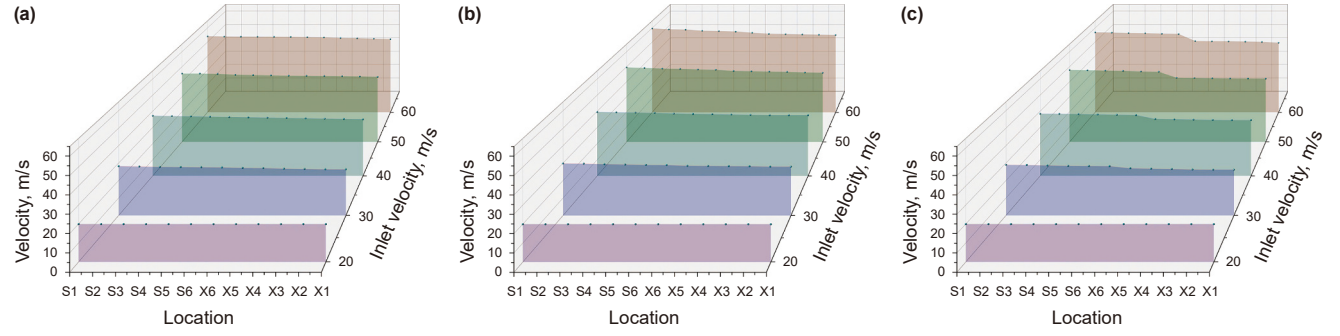


Fig. 14. Temperature at different positions of the cross-section. **(a)** Upper wall, **(b)** section center, **(c)** lower wall.

upper wall of section S1. In the upward-inclined segment, the highest velocity is observed at the section center, corresponding to the maximum mass transfer coefficient. In the downward-inclined segment, the lowest local velocity occurs at the lower wall, where the mass transfer coefficient is minimized. Reduced local velocity weakens the concentration gradient, thereby decreasing both the mass transfer coefficient and the corrosion rate. The combined action of the bend and the slope produces different near-wall wetting patterns, secondary-flow intensities, and shear stresses in the two segments. On the upward-inclined segment, gravity-induced stratification is superimposed on the curvature-induced Dean secondary flow. Stronger local shear and radial convection occur at the pipe top, and the concentration boundary layer is thinner. On the downward-inclined segment, the near-wall liquid film tends toward a quasi-continuous state, and the shear is relatively steady. When the inlet velocity changes, the Dean number in the pipe changes accordingly. The secondary flow pattern therefore varies. A higher Dean number corresponds to stronger secondary flow. The secondary flow alters the local mass transfer coefficients along the pipe wall and the radial velocity field in the fluid. These changes modify the concentration gradients of corrosion products at the wall and thus the local corrosion behavior. Consequently, an increase in the Dean number makes the flow in the pipe more unsteady. It may not only raise the overall corrosion level but also amplify spatial differences in corrosion intensity. Consistent with the CFD results of turbulent kinetic

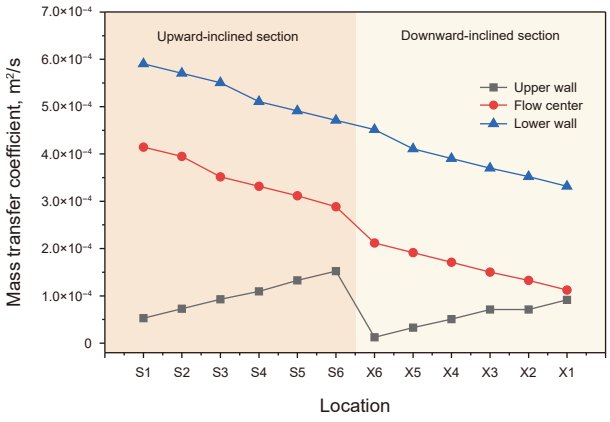


Fig. 15. Mass transfer coefficients at different locations.

energy and wall shear stress, TKE and shear stress are higher at the lower wall of the upward-inclined segment and the upper wall of the downward-inclined segment, leading to more severe corrosion at these locations.

3.7. Corrosion rate monitored by probes

Fig. 16 shows the polarization curves of probes after 36 h of loop flow at different inlet velocities, with fitted Tafel parameters listed in Table 4. The Tafel equations are presented in Eqs. (10)–(12), with the anode and cathode Tafel slopes denoted as b_a and b_c, respectively. The corrosion potential (E_{corr}), indicating the tendency of the electrode surface to corrode, and the corrosion current density (I_{corr}), representing the corrosion rate, are affected by flow velocity. With increasing velocity, E_{corr} of both the pipe wall and internal probes first shifts negatively, then positively. The cathodic Tafel slope (b_c) is substantially higher than the anodic Tafel slope (b_a), indicating cathodically controlled corrosion, with the cathodic reaction enhanced by flow. Under high Cl^- concentrations and high CO_2 environments, the cathodic process (such as H^+ reduction) tends to become diffusion/mass-transfer controlled under flow conditions. Flow-induced erosion also leads to the breakdown of the protective film, which enhances the cathodic reaction, resulting in $b_c > b_a$. Below 0.8 m/s, the Tafel slope of internal probes (T1, T2) are lower than those of the pipe wall, and I_{corr} decreases slightly with velocity. Above 0.8 m/s, the internal probe constants exceed those of the pipe wall, and I_{corr} increases sharply, reflecting weakened film protection and accelerated corrosion.

$$\eta = a + b \times \log(i) \tag{10}$$

$$b_a = \frac{2.303RT}{\alpha_a nF} \tag{11}$$

$$b_c = \frac{2.303RT}{\alpha_c nF} \tag{12}$$

In inclined pipelines, the probe-measured corrosion rate initially decreases and then increases with flow velocity. The maximum rate of 3.9831 mm/a occurs at 1.2 m/s, while the minimum of 0.2504 mm/a appears at 0.8 m/s. At velocities below 0.8 m/s, low shear limits corrosion product removal and ion transport, promoting the formation of a dense protective film and reducing the corrosion rate. When velocity exceeds 0.8 m/s, intensified shear induces substantial film detachment, creating potential differences that trigger autocatalytic galvanic corrosion, while enhanced mass transfer delivers more corrosive ions to the base metal, accelerating corrosion.

Fig. 17 presents polarization curves of probes at different locations after 36 h of loop flow under varying temperatures, with extrapolated Tafel fitting results summarized in Table 5. Both fluid temperature and probe location significantly influence corrosion. I_{corr} increases with temperature, indicating intensified probe surface corrosion and dissolution of the protective film. The cathodic Tafel slope (b_c) exceeds the anodic constant (b_a), indicating a cathodically controlled process with diffusion-limited cathodic polarization and active anodic dissolution. With increasing temperature, b_a shows minor variation ([56.45, 167.25]), whereas b_c rises markedly ([91.52, 546.13]), demonstrating that temperature primarily accelerates the cathodic reaction of 20# steel.

In the inclined pipeline, the probe-measured corrosion rate gradually increases with temperature. The maximum rate of 1.9428 mm/a occurs at 60 °C, and the minimum of 0.0884 mm/a at 20 °C. In the upward-inclined segment, T1 exhibits generally lower corrosion than the pipe wall, with peak wall corrosion at point A. In the downward-inclined segment, T2 corrosion consistently exceeds that of the pipe wall, peaking at point D. Elevated temperatures enhance H^+ and Cl^- ion activity, facilitating their penetration through the corrosion product film and accumulation on the base metal. The film dissolution rate surpasses $FeCO_3$ precipitation, transforming the dense layer into a porous structure that is partially removed by fluid scouring, exposing the base metal to active dissolution and accelerating probe corrosion.

After 12, 24, and 36 h of flow corrosion, the polarization curves of probes at different positions are shown in Fig. 18, with fitted results summarized in Table 6. I_{corr} gradually decreases with exposure time, indicating reduced probe corrosion and progressive formation of corrosion product films. The cathodic Tafel slope (b_c) remains larger than the anodic Tafel slope (b_a), reflecting cathodically controlled corrosion. Cathodic polarization is diffusion-controlled, whereas the anodic reaction proceeds via active dissolution. Over time, b_a varies slightly (82.76–167.19), while b_c changes significantly (263.91–656.13), confirming that corrosion predominantly occurs via the cathodic reaction and that product film formation mitigates metal dissolution.

In the inclined pipeline, probe-measured corrosion rates initially decrease rapidly and then decline gradually over time. At 12 h, the maximum corrosion rate of 7.00 mm/a indicates severe corrosion, decreasing to 1.91 mm/a at 36 h. Early-stage corrosion is intense at low potentials, with rapid ion exchange promoting corrosion and formation of corrosion product films. High fluid shear continuously strips these films, causing uneven coverage and localized galvanic corrosion, accelerating the corrosion rate. Over time, film formation slightly exceeds dissolution, gradually covering the surface and reducing corrosion. In the upward-inclined segment, corrosion rates follow T1 > B > A, whereas in the downward-inclined segment they follow T2 > C > D.

3.8. Probe monitoring effectiveness

The corrosion monitoring effectiveness was defined as the ratio of probe-measured corrosion rate to the circumferential maximum wall corrosion rate at the same cross-section. The effectiveness of internal probes T1 and T2 under varying flow velocities and temperatures is presented in Fig. 19. Probe effectiveness initially increased and then decreased with rising flow velocity, peaking at 0.8 m/s in the upward-inclined segment (72.88%) and reaching a minimum at 1.2 m/s in the downward-inclined segment (50.10%). Effectiveness in the upward-inclined segment was consistently higher than in the downward-inclined segment, with an average difference of 6.95%, which widened with increasing flow velocity. As

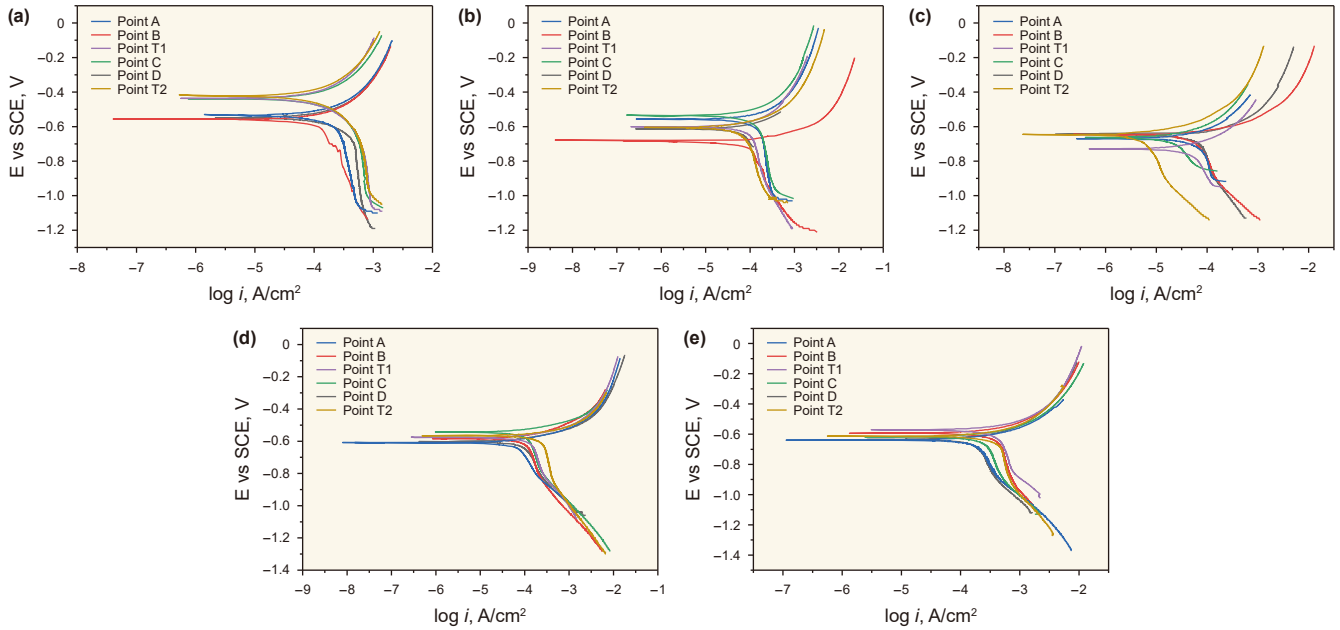


Fig. 16. Polarization curves of probes at different flow velocities and installation positions. **(a)** $v = 0.4$ m/s, **(b)** $v = 0.6$ m/s, **(c)** $v = 0.8$ m/s, **(d)** $v = 1.0$ m/s, **(e)** $v = 1.2$ m/s. E represents the electrode potential, and SCE refers to the saturated calomel electrode.

Table 4
Fitted values of polarization curves at different monitoring points under varying inlet flow velocities.

Flow velocity, m/s	Monitoring location		b_a, mV/decade	b_c, mV/decade	E_{corr}, V	I_{corr}, A/cm^2	V_{corr}, mm/a
0.4	Upward-inclined segment	A	169.93 ± 4.04	272.38 ± 5.71	−0.5302 ± 0.01	(1.18 ± 0.03) × 10^{-4}	1.37
		T1	175.96 ± 5.38	192.68 ± 4.10	−0.4343 ± 0.03	(7.99 ± 0.05) × 10^{-5}	0.93
		B	167.76 ± 3.83	273.02 ± 8.26	−0.5591 ± 0.02	(1.02 ± 0.01) × 10^{-4}	1.19
	Downward-inclined segment	C	168.68 ± 2.95	208.62 ± 11.08	−0.4342 ± 0.04	(8.95 ± 0.01) × 10^{-5}	1.04
		T2	172.54 ± 1.73	202.30 ± 4.80	−0.4192 ± 0.02	(7.98 ± 0.02) × 10^{-5}	0.93
		D	169.92 ± 3.36	221.36 ± 15.97	−0.5433 ± 0.01	(1.21 ± 0.04) × 10^{-4}	1.39
0.6	Upward-inclined segment	A	160.94 ± 2.61	427.47 ± 9.19	−0.5638 ± 0.05	(1.11 ± 0.02) × 10^{-4}	1.39
		T1	158.50 ± 2.33	485.45 ± 12.61	−0.6072 ± 0.04	(8.26 ± 0.01) × 10^{-5}	0.96
		B	87.34 ± 4.09	312.46 ± 5.68	−0.7134 ± 0.02	(9.74 ± 0.01) × 10^{-5}	1.14
	Downward-inclined segment	C	149.46 ± 5.46	369.28 ± 8.76	−0.5334 ± 0.04	(9.11 ± 0.02) × 10^{-5}	1.06
		T2	123.39 ± 3.09	349.75 ± 8.47	−0.6200 ± 0.01	(5.39 ± 0.01) × 10^{-5}	0.93
		D	136.68 ± 3.98	433.30 ± 11.71	−0.6130 ± 0.02	(1.39 ± 0.05) × 10^{-4}	1.44
0.8	Upward-inclined segment	A	162.70 ± 2.76	376.13 ± 5.32	−0.6698 ± 0.01	(6.07 ± 0.04) × 10^{-5}	0.71
		T1	138.80 ± 2.66	413.89 ± 4.87	−0.7283 ± 0.03	(4.43 ± 0.02) × 10^{-5}	0.52
		B	104.32 ± 1.69	292.68 ± 8.51	−0.6834 ± 0.02	(5.01 ± 0.01) × 10^{-5}	0.60
	Downward-inclined segment	C	134.92 ± 4.31	325.98 ± 9.74	−0.6772 ± 0.05	(2.13 ± 0.01) × 10^{-5}	0.25
		T2	100.51 ± 4.76	439.54 ± 5.40	−0.6689 ± 0.01	(8.25 ± 0.03) × 10^{-5}	0.97
		D	121.21 ± 2.23	475.51 ± 11.30	−0.6729 ± 0.01	(6.26 ± 0.01) × 10^{-5}	0.73
1.0	Upward-inclined segment	A	91.72 ± 1.83	384.35 ± 3.73	−0.6255 ± 0.04	(6.80 ± 0.01) × 10^{-5}	0.80
		T1	82.21 ± 4.00	635.24 ± 7.70	−0.5769 ± 0.05	(1.34 ± 0.04) × 10^{-4}	1.57
		B	116.47 ± 2.67	510.42 ± 5.90	−0.6007 ± 0.02	(1.01 ± 0.06) × 10^{-4}	1.17
	Downward-inclined segment	C	89.97 ± 5.34	548.41 ± 13.99	−0.5585 ± 0.03	(1.07 ± 0.05) × 10^{-4}	1.25
		T2	81.53 ± 3.90	314.53 ± 13.48	−0.5660 ± 0.01	(1.62 ± 0.03) × 10^{-4}	1.79
		D	82.07 ± 4.23	388.65 ± 3.76	−0.6086 ± 0.01	(8.47 ± 0.01) × 10^{-5}	0.99
1.2	Upward-inclined segment	A	131.02 ± 2.62	420.18 ± 6.51	−0.6578 ± 0.03	(1.66 ± 0.03) × 10^{-4}	1.95
		T1	161.86 ± 3.47	454.91 ± 9.37	−0.5875 ± 0.04	(3.37 ± 0.02) × 10^{-4}	3.93
		B	157.73 ± 2.85	521.73 ± 7.64	−0.5974 ± 0.02	(3.27 ± 0.02) × 10^{-4}	2.93
	Downward-inclined segment	C	145.31 ± 2.67	521.11 ± 3.60	−0.6369 ± 0.01	(2.28 ± 0.01) × 10^{-4}	2.66
		T2	164.71 ± 2.98	573.99 ± 7.26	−0.6136 ± 0.03	(3.40 ± 0.01) × 10^{-4}	3.99
		D	151.23 ± 1.55	429.63 ± 5.14	−0.6616 ± 0.01	(1.64 ± 0.01) × 10^{-4}	1.91

the inlet velocity rises from 0.4 to 0.8 m/s, wall shear stress and TKE increase. The near-wall film becomes continuous, and wettability/connectivity improve. The boundary layer thins and mass transfer increases, enhancing transport of cathodic reactants and products. At this stage, center and wall show similar gains in the convective mass transfer coefficient. The low-velocity bias from insufficient wetting/connectivity decreases substantially, so monitoring effectiveness rises. As the velocity approaches 0.8 m/s, connectivity saturates and monitoring effectiveness reaches a peak. Increasing the velocity to 1.2 m/s strengthens curvature-induced secondary flow. The near-wall boundary layer thins further, circumferential and radial convection intensify, and shear erosion of the film increases. The rise in TKE at the wall then exceeds that at the center. The actual wall corrosion rate grows superlinearly, while the center-probe rate increases only modestly. Monitoring effectiveness therefore declines.

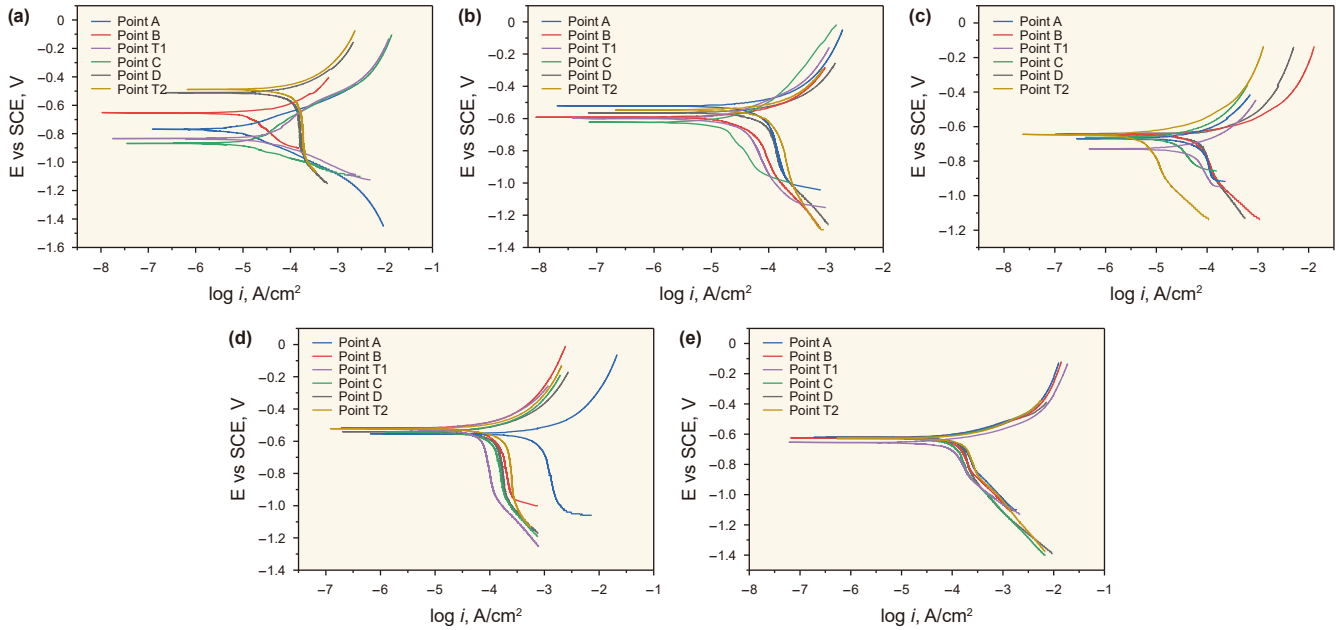


Fig. 17. Polarization curves of probes at different installation positions under varying temperatures. **(a)** $T = 20$ °C, **(b)** $T = 30$ °C, **(c)** $T = 40$ °C, **(d)** $T = 50$ °C, **(e)** $T = 60$ °C.

Table 5
Fitted values of polarization curves at each monitoring point under different medium temperatures.

Temperature, °C	Monitoring location		b_a, mV/decade	b_c, mV/decade	E_{corr}, V	I_{corr}, A/cm²	V_{corr}, mm/a
20	Upward-inclined segment	A	118.65 ± 5.72	139.58 ± 7.58	−0.7736 ± 0.01	(7.58 ± 0.03) × 10^{-6}	0.09
		T1	154.22 ± 3.12	104.40 ± 3.61	−0.8340 ± 0.01	(2.12 ± 0.01) × 10^{-5}	0.22
		B	143.63 ± 3.16	179.62 ± 10.11	−0.7087 ± 0.01	(1.48 ± 0.02) × 10^{-5}	0.17
	Downward-inclined segment	C	167.25 ± 2.25	115.53 ± 11.97	−0.8699 ± 0.02	(1.31 ± 0.04) × 10^{-5}	0.15
		T2	149.10 ± 4.23	366.38 ± 3.92	−0.4902 ± 0.01	(7.45 ± 0.05)×10^{-5}	0.87
		D	142.59 ± 3.08	353.44 ± 4.73	−0.5127 ± 0.03	(6.72 ± 0.01) × 10^{-5}	0.78
30	Upward-inclined segment	A	140.36 ± 2.62	277.10 ± 4.40	−0.5380 ± 0.02	(4.53 ± 0.01) × 10^{-5}	0.43
		T1	106.33 ± 3.84	152.79 ± 4.70	−0.6015 ± 0.05	(1.03 ± 0.02) × 10^{-5}	0.31
		B	97.61 ± 3.45	353.90 ± 6.01	−0.5922 ± 0.03	(2.67 ± 0.01) × 10^{-5}	0.31
	Downward-inclined segment	C	133.16 ± 3.09	350.87 ± 4.84	−0.6257 ± 0.01	(1.34 ± 0.03) × 10^{-5}	0.16
		T2	154.68 ± 3.45	370.79 ± 7.20	−0.5543 ± 0.03	(6.57 ± 0.05) × 10^{-5}	0.77
		D	132.13 ± 5.23	321.28 ± 8.27	−0.5760 ± 0.02	(5.17 ± 0.01) × 10^{-5}	0.67
40	Upward-inclined segment	A	162.70 ± 1.80	376.13 ± 4.36	−0.6698 ± 0.04	(6.07 ± 0.02) × 10^{-5}	0.71
		T1	138.80 ± 3.36	413.89 ± 3.41	−0.7283 ± 0.01	(4.43 ± 0.04) × 10^{-5}	0.52
		B	104.32 ± 1.61	292.68 ± 4.14	−0.6834 ± 0.05	(5.10 ± 0.04) × 10^{-5}	0.60
	Downward-inclined segment	C	134.92 ± 1.60	325.98 ± 10.36	−0.6772 ± 0.03	(2.13 ± 0.02) × 10^{-5}	0.25
		T2	100.51 ± 2.14	439.54 ± 6.73	−0.6689 ± 0.05	(8.25 ± 0.01) × 10^{-5}	0.96
		D	121.21 ± 3.38	475.51 ± 7.59	−0.6729 ± 0.04	(6.26 ± 0.03) × 10^{-5}	0.73
50	Upward-inclined segment	A	56.45 ± 2.68	91.52 ± 8.99	−0.5543 ± 0.02	(7.79 ± 0.03) × 10^{-5}	0.91
		T1	135.97 ± 2.14	412.29 ± 4.37	−0.5335 ± 0.01	(4.77 ± 0.01) × 10^{-5}	0.66
		B	159.06 ± 2.26	334.74 ± 8.32	−0.5219 ± 0.02	(7.10 ± 0.02) × 10^{-5}	0.83
	Downward-inclined segment	C	140.13 ± 1.61	402.66 ± 7.42	−0.5488 ± 0.01	(7.08 ± 0.05) × 10^{-5}	0.83
		T2	156.73 ± 3.55	324.39 ± 5.26	−0.5235 ± 0.03	(9.54 ± 0.05) × 10^{-5}	1.27
		D	139.01 ± 4.62	416.44 ± 12.45	−0.5450 ± 0.01	(8.30 ± 0.01) × 10^{-5}	0.97
60	Upward-inclined segment	A	104.84 ± 4.46	413.26 ± 6.54	−0.6203 ± 0.05	(1.12 ± 0.03) × 10^{-4}	1.31
		T1	67.34 ± 5.09	224.75 ± 3.71	−0.6563 ± 0.04	(5.07 ± 0.01) × 10^{-5}	0.59
		B	102.99 ± 3.19	457.67 ± 4.74	−0.6273 ± 0.05	(9.90 ± 0.01) × 10^{-5}	1.16
	Downward-inclined segment	C	107.98 ± 2.86	402.79 ± 8.34	−0.6454 ± 0.03	(8.74 ± 0.02) × 10^{-5}	1.02
		T2	130.73 ± 3.18	525.49 ± 13.07	−0.6408 ± 0.02	(1.46 ± 0.01) × 10^{-4}	1.94
		D	119.91 ± 3.06	546.13 ± 7.48	−0.6422 ± 0.05	(1.25 ± 0.03) × 10^{-4}	1.46

Temperature elevation caused a gradual decrease in effectiveness, with the maximum observed at 20 °C for T1 in the upward-inclined segment (74.63%) and the minimum at 60 °C for T2 in the downward-inclined segment (67.00%), yielding an average difference of 3.93% between segments. CFD simulations indicated that higher temperatures increased the temperature difference between the wall and the fluid, particularly in the downward-inclined segment, reducing probe effectiveness, consistent with experimental results. As temperature rises, viscosity falls. At the same inlet velocity, the Reynolds number and wall shear increase. The Schmidt number decreases and diffusion strengthens, raising the convective mass transfer coefficient, especially at the wall due to a thinner boundary layer and stronger circumferential/radial convection. Additionally, heating accelerates cathodic kinetics, destabilizes the $FeCO_3$ film, and promotes its shear removal. Wall corrosion becomes more temperature-sensitive. Consequently, monitoring effectiveness declines. Calculations further show larger wall–fluid temperature differences and greater flow-regime

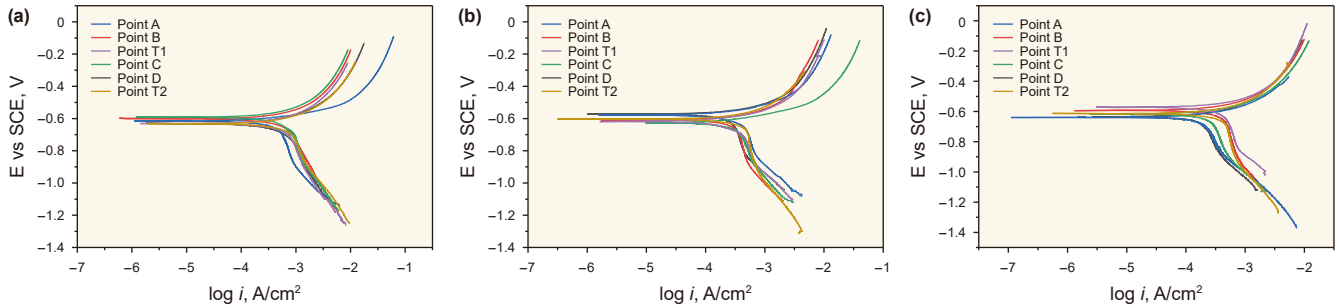


Fig. 18. Polarization curves of the probe at different installation positions and times. **(a)** t = 12 h, **(b)** t = 24 h, **(c)** t = 36 h.

Table 6
Fitted polarization curve values at different experimental durations.

Time, h	Monitoring location		b_a, mV/decade	b_c, mV/decade	E_{corr}, V	I_{corr}, A/cm^2	V_{corr}, mm/a
12	Upward-inclined segment	A	82.76 ± 2.73	422.98 ± 6.06	0.6209 ± 0.01	(3.59 ± 0.03) × 10^{-4}	3.61
		T1	158.08 ± 2.79	375.24 ± 4.60	−0.6278 ± 0.03	(4.49 ± 0.01) × 10^{-4}	6.00
		B	156.72 ± 4.78	322.18 ± 6.86	−0.6033 ± 0.01	(4.37 ± 0.01) × 10^{-4}	3.81
	Downward-inclined segment	C	156.09 ± 1.53	306.53 ± 7.06	−0.5883 ± 0.02	(4.20 ± 0.02) × 10^{-4}	4.40
		T2	148.42 ± 2.18	389.50 ± 8.08	−0.6263 ± 0.01	(5.22 ± 0.01) × 10^{-4}	7.00
		D	137.62 ± 2.42	263.91 ± 9.14	−0.6375 ± 0.05	(3.61 ± 0.03) × 10^{-4}	4.20
24	Upward-inclined segment	A	118.34 ± 5.19	350.28 ± 7.03	−0.5811 ± 0.02	(2.65 ± 0.01) × 10^{-4}	2.79
		T1	124.75 ± 2.63	501.89 ± 6.37	−0.6181 ± 0.04	(3.15 ± 0.02) × 10^{-4}	4.20
		B	152.90 ± 4.15	626.04 ± 6.50	−0.6256 ± 0.06	(2.78 ± 0.01) × 10^{-4}	2.94
	Downward-inclined segment	C	84.40 ± 3.28	488.62 ± 5.37	−0.6241 ± 0.03	(2.69 ± 0.01) × 10^{-4}	3.15
		T2	167.19 ± 3.97	656.13 ± 9.44	−0.5987 ± 0.02	(3.67 ± 0.03) × 10^{-4}	4.77
		D	141.39 ± 3.80	465.40 ± 12.77	−0.5971 ± 0.01	(2.31 ± 0.02) × 10^{-3}	2.69
36	Upward-inclined segment	A	131.02 ± 2.74	420.18 ± 4.06	−0.6578 ± 0.01	(1.66 ± 0.01) × 10^{-4}	1.95
		T1	161.86 ± 3.54	454.91 ± 8.57	−0.5875 ± 0.02	(3.37 ± 0.03) × 10^{-4}	3.93
		B	157.73 ± 1.92	521.73 ± 7.66	−0.5974 ± 0.03	(3.27 ± 0.03) × 10^{-4}	2.93
	Downward-inclined segment	C	145.31 ± 3.69	521.11 ± 4.46	−0.6369 ± 0.03	(2.28 ± 0.02) × 10^{-4}	2.66
		T2	164.71 ± 1.84	573.99 ± 4.33	−0.6136 ± 0.01	(3.40 ± 0.01) × 10^{-4}	3.98
		D	151.23 ± 3.01	429.63 ± 3.18	−0.6616 ± 0.04	(1.64 ± 0.01) × 10^{-4}	1.91

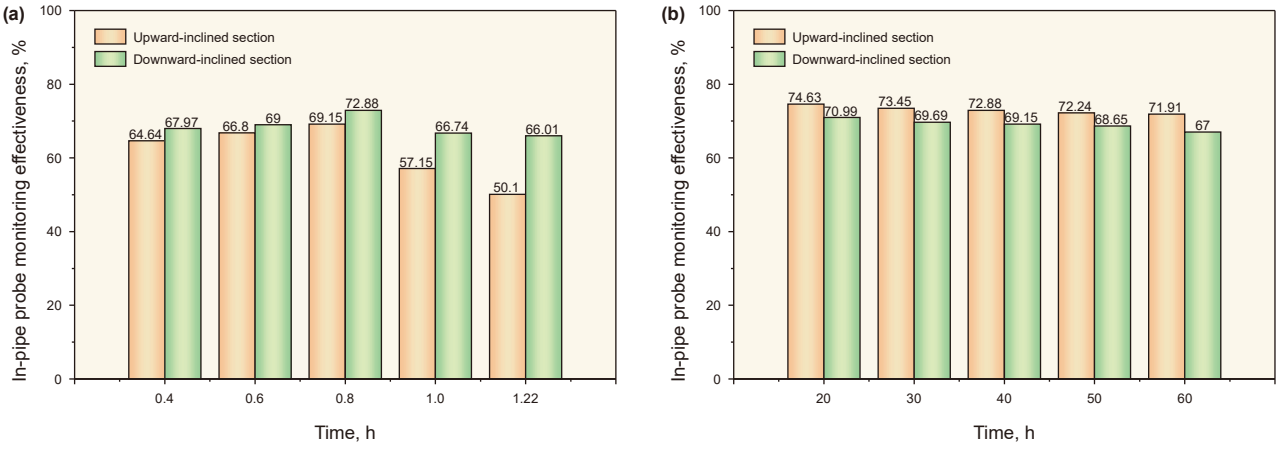


Fig. 19. Corrosion monitoring effectiveness of probes under different conditions. **(a)** Varying flow velocities, **(b)** varying temperatures.

asymmetry in the downward-inclined segment, which amplify wall mass transfer and film stripping and yield lower monitoring effectiveness than in the upward-inclined segment.

Internal probe corrosion monitoring effectiveness at different durations is shown in Fig. 20. Probe effectiveness in the upward-inclined segment was slightly higher than in the downward-inclined segment, with an average difference of approximately 5.5%. Effectiveness rose rapidly from 5.15% at 12 h to 62.75% at 24 h, and then more gradually to 76.48% at 36 h. Early corrosion was dominated by pitting nucleation, while by 36 h pits had expanded and coalesced, and corrosion product films had formed, slowing the process. Thus, a 36 h monitoring period is recommended.

4. Discussion

4.1. Corrected corrosion probe monitoring effectiveness charts

Based on corrections for flow velocity and temperature, a corrosion rate prediction model applicable to different pipe locations and azimuthal positions was established. Linear regression was applied

using CFD–derived hydrodynamic parameters from six monitoring points (upper wall A and C, mid-section T1 and T2, lower wall B and D) across 12 sections (S1–S6, X1–X6) to develop velocity- and temperature-corrected models for each point. For the velocity-correction model, three location types were selected at each of the twelve cross-sections: upper wall, lower wall, and in-pipe probe. This yielded $N = 180$ data points under the corresponding operating-condition combinations. For the temperature-correction model, the CFD temperature field indicates that the difference between the probe center and the adjacent near-wall fluid is negligible, whereas a clear difference exists between the upper and lower walls. Therefore, the upper and lower walls were used as representative points, producing 120 data points under the same twelve cross-sections and operating-condition combinations. The corresponding calculation formulas are presented in Eqs. (13) and (14).

$$\begin{bmatrix} 1 & L_1 & v_1 \\ \dots & \dots & \dots \\ 1 & L_{180} & v_{180} \end{bmatrix} \times [\ \varepsilon_1 \quad A \quad B\ ]^{\mathrm{T}} = [\ V_1 \quad \dots \quad \dots \quad V_{180}\ ]^{\mathrm{T}} \tag{13}$$

$$\begin{bmatrix} 1 & L_1 & T_1 \\ \dots & \dots & \dots \\ 1 & L_{120} & T_{120} \end{bmatrix} \times [\ \varepsilon_2 \quad E \quad Q\ ]^{\mathrm{T}} = [\ T_1 \quad \dots \quad \dots \quad T_{120}\ ]^{\mathrm{T}} \tag{14}$$

Using linear regression combined with CFD-simulated local flow fields, velocity correction models were established for the upper wall, pipe interior, and lower wall in both the upward- and downward-inclined segments. Due to heat conduction between the pipe wall and air, near-wall fluid exhibits a temperature difference from the pipe interior. Applying the same method, four temperature correction models were derived-upper and lower walls of both inclined segments-suitable for temperature adjustments in high-water-cut crude oil gathering pipelines with elevation changes. Probe monitoring experiments indicated that local corrections of velocity v, fluid temperature T, and experimental time t significantly affect monitoring effectiveness. Thus, the corrosion rate prediction model is expressed in Eq. (15).

$$v_{\mathrm{corr}} = m \cdot f(T, t, v) \tag{15}$$

In the equation, f is a function of the factors T, t, and v, which are defined as follows: $\ln(V_{\mathrm{corr}}) = \frac{BE_a}{RT}$, $\ln(V_{\mathrm{corr}}) = \ln C\left(\frac{\rho v d}{\mu}\right)$, $\ln(V_{\mathrm{corr}}) = \ln(D \ln(t+1))$.

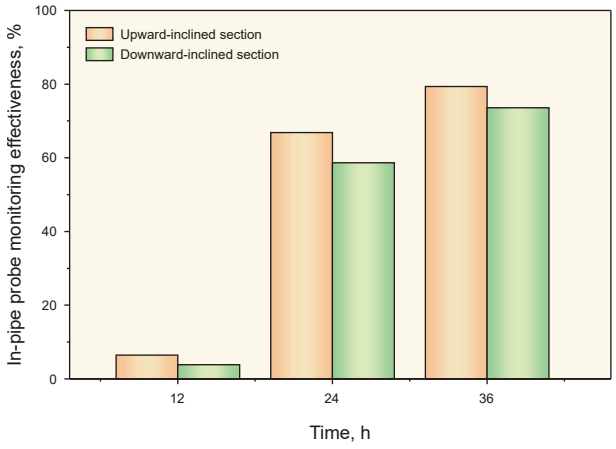


Fig. 20. Corrosion monitoring effectiveness of internal probes at different durations.

Therefore, the corrected corrosion rate model is expressed as Eq. (16).

$$v_{\mathrm{corr}} = M \cdot e^{\frac{BE_a}{RT}} \cdot \left(\frac{\rho v d}{\mu}\right) \cdot \ln(t+1) \tag{16}$$

Based on probe monitoring effectiveness experiments, the corrected temperature T, flow velocity v, and experimental time t were input into a MATLAB multiple linear regression to derive Eq. (17), establishing corrosion rate prediction models for both internal probes and pipe walls in the upward-inclined and downward-inclined segments. Comparison of probe and wall corrosion rates then yielded the corrosion monitoring correction model.

$$\begin{bmatrix} 1 & \frac{E_a}{RT_1} & \ln V_1 & \ln(t_1+1) \\ \dots & \dots & \dots & \dots \\ \dots & \dots & \dots & \dots \\ 1 & \frac{E_a}{RT_{66}} & \ln V_{66} & \ln(t_{66}+1) \end{bmatrix} \times [\ \varepsilon_3 \quad E \quad Q \quad G\ ]^{\mathrm{T}} = [\ \ln V_{\mathrm{corr1}} \quad \dots \quad \dots \quad \ln V_{\mathrm{corr66}}\ ]^{\mathrm{T}} \tag{17}$$

Using MATLAB multiple linear regression, corrosion rate prediction models were established for six locations, the upper wall, internal probe, and lower wall of both the upward-inclined and downward-inclined segments. The results are presented in Table 7.

The effectiveness correction model relating pipe wall corrosion rate to probe-monitored corrosion rate is expressed in Eq. (18). Based on the corrosion rate prediction models, the effectiveness correction models under different flow velocities and pipe locations were obtained, as summarized in Table 8.

$$n = \frac{V_{\mathrm{corrwall}} - V_{\mathrm{corrprobe}}}{V_{\mathrm{corrwall}}} \tag{18}$$

The corrected chart for probe monitoring effectiveness is shown in Fig. 21. This model applies to high-water-cut crude oil gathering pipelines with ±45° inclinations, a 108 mm inner diameter, and 20# steel construction. The applicable medium conditions are characterized by a water cut exceeding 92% (up to 100%), no H_2S, a CO_2 partial pressure of 0.8 MPa, a NaCl concentration of 50000 mg/L, temperatures of 20–60 °C, and flow velocities of 0.4–1.2 m/s. Fig. 21 (a) corresponds to flow velocities of [0.4, 0.8] m/s, while Fig. 21 (b) applies to (0.8, 1.2] m/s. If applied under other operating conditions (e.g., with H_2S present, a lower water cut, or a different CO_2 partial pressure), the model must be recalibrated, similarity verified using dimensionless criteria, and application-specific checks performed before deployment.

4.2. Field application

A high-water-cut crude oil gathering pipeline with 45° upward- and −45° downward-inclined segments, 108 mm diameter, and 20# steel construction was used for field testing with an ER7100 resistance probe. Produced water (100% water cut, no oil phase, H_2S-free, CO_2 0.8 MPa, NaCl 50000 mg/L) at 40 °C and 0.6 m/s flow served as the test medium. Corrected monitoring charts were applied for one month with 36 h data intervals. At the start and end of each experiment, co-located ultrasonic thickness (UT) measurements were taken with a CTS-30A gauge (0.80–300.0 mm; ±0.01/±0.1 mm) to obtain baseline and final wall thicknesses. Corrosion rate was computed as thickness loss divided by exposure time. Per cross-section (0.40 m from the elbow), eight circumferential points were set every 45°, and five axial positions were laid out within ±0.20 m at 0.10 m spacing. The upward-

Table 7
Corrosion rate prediction models for different locations.

Velocity correction model	Temperature correction model	Corrosion rate prediction model
$V_{UU} = 0.0310 \times L + 0.6981 \times v - 0.1493$	$T_{UU} = -0.1707 \times L + 0.8602 \times T_0 + 2.6667$	$V_{corrUU} = 0.0211 \cdot e^{\frac{-0.5348E_a}{RT}} \cdot \left(\frac{\rho v d}{\mu}\right) \cdot \ln(t+1)$
$V_{UP} = -0.0260 \times L + 0.9341 \times v + 0.1552$	–	$V_{corrUP} = 3.1291 \cdot 10^{-4} \cdot e^{\frac{-0.1384E_a}{RT}} \cdot \left(\frac{\rho v d}{\mu}\right) \cdot \ln(t+1)$
$V_{UL} = -0.0194 \times L + 0.9681 \times v + 0.0504$	$T_{UL} = -0.2089 \times L + 0.9210 \times T_0 + 1.8066$	$V_{corrUL} = 1.8281 \cdot 10^{-9} \cdot e^{\frac{0.9694E_a}{RT}} \cdot \left(\frac{\rho v d}{\mu}\right) \cdot \ln(t+1)$
$V_{DU} = 0.0192 \times L + 0.8581 \times v - 0.0737$	$T_{DU} = 0.2034 \times L + 0.8608 \times T_0 + 0.2122$	$V_{corrDU} = 6.0093 \cdot 10^{-9} \cdot e^{\frac{0.8516E_a}{RT}} \cdot \left(\frac{\rho v d}{\mu}\right) \cdot \ln(t+1)$
$V_{DP} = 0.0168 \times L + 1.0757 \times v - 0.0806$	–	$V_{corrDP} = 1.7101 \cdot 10^{-9} \cdot e^{\frac{E_a}{RT}} \cdot \left(\frac{\rho v d}{\mu}\right) \cdot \ln(t+1)$
$V_{DL} = -0.0190 \times L + 0.7430 \times v + 0.0058$	$T_{DL} = 0.1650 \times L + 0.7849 \times T_0 + 2.5353$	$V_{corrDL} = 1.8749 \cdot 10^{-9} \cdot e^{\frac{E_a}{RT}} \cdot \left(\frac{\rho v d}{\mu}\right) \cdot \ln(t+1)$

Table 8
Effectiveness correction models at different flow velocities and pipe locations.

Sequence number	Flow velocity, m/s	Location	Effectiveness correction models
1	[0.4,0.8]	Upward-inclined segment	$n_{\text{upward-inclined section}} = 1 - 0.0148 \cdot \frac{Re_{probe}}{Re_{wall}} \cdot e^{\frac{E_a}{R}\left(\frac{0.5348}{T_{wall}} - \frac{0.1384}{T_{probe}}\right)}$
2		Downward-inclined segment	$n_{\text{downward-inclined section}} = 1 - 0.0912 \cdot \frac{Re_{probe}}{Re_{wall}} \cdot e^{\frac{E_a}{R}\left(\frac{1}{T_{probe}} - \frac{1}{T_{wall}}\right)}$
3	(0.8,1.2]	Upward-inclined segment	$n_{\text{upward-inclined section}} = 1 - 1.7117 \cdot 10^{5} \cdot \frac{Re_{probe}}{Re_{wall}} \cdot e^{\frac{E_a}{R}\left(\frac{0.9694}{T_{wall}} + \frac{0.1384}{T_{probe}}\right)}$
4		Downward-inclined segment	$n_{\text{downward-inclined section}} = 1 - 0.2846 \cdot \frac{Re_{probe}}{Re_{wall}} \cdot e^{\frac{E_a}{R}\left(\frac{1}{T_{probe}} - \frac{0.8516}{T_{wall}}\right)}$

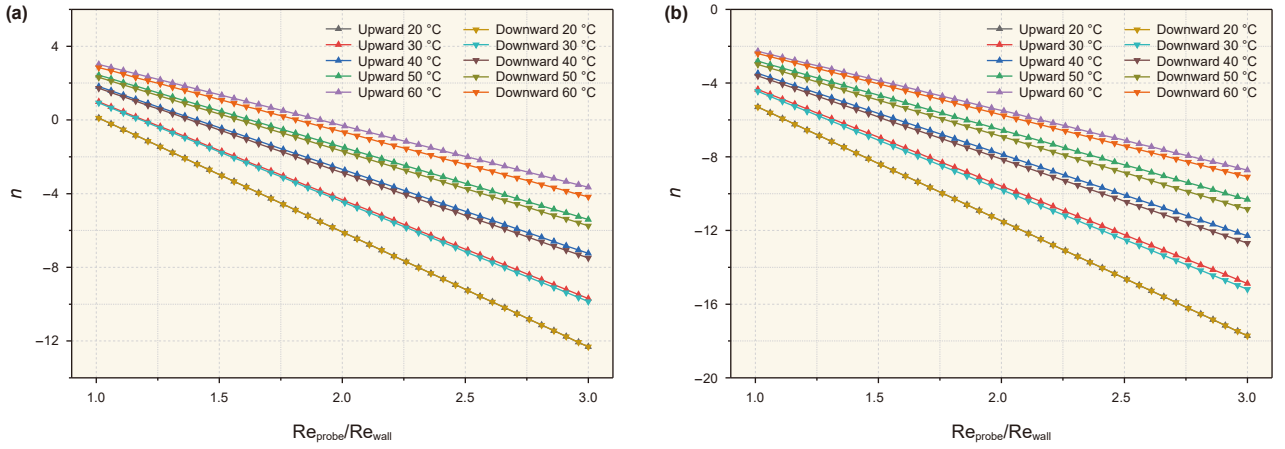


Fig. 21. Corrected charts for probe monitoring effectiveness. **(a)** Flow velocity [0.4, 0.8] m/s, **(b)** flow velocity (0.8, 1.2] m/s.

inclined and downward-inclined segments contained 40 points each (80 total). Each point was measured three times and averaged. Before measurement, sound velocity and zero were calibrated with a 20# steel reference block, with temperature compensation at field conditions. Test areas were cleaned to bare metal. For each cross-section, the reference wall corrosion rate was the maximum of the eight circumferential points. This value was paired with the probe reading at the same section to compute monitoring effectiveness and the improvement after correction. Correction charts were selected by flow velocity, and the Reynolds number ratio determined the correction factor n, as shown in Fig. 22. Post-correction, monitoring effectiveness reached 97.36% (upward) and 93.83% (downward), with an average improvement of 35.72%, as shown in Table 9.

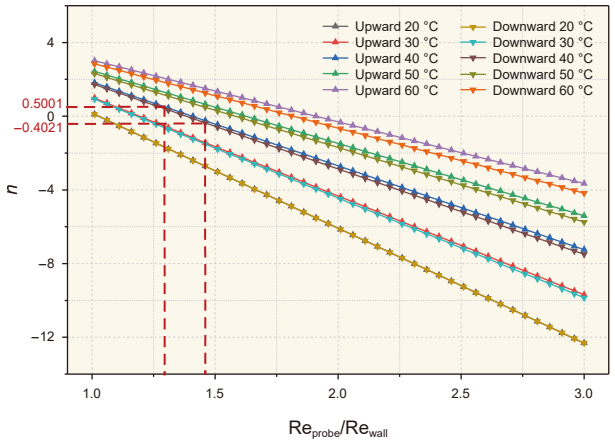


Fig. 22. Application of the corrected chart for probe monitoring effectiveness at flow velocities of [0.4, 0.8] m/s.

Table 9
Application of the corrected chart in a high-water-cut crude oil pipeline with elevation changes.

Sequence number	Parameter	Upward-inclined probe	Downward-inclined probe
1	Original probe-measured rate, mm/a	0.6001	1.8292
2	Actual pipeline corrosion rate, mm/a	1.1696	1.3904
Monitoring effectiveness, %		51.31	68.44
3	Re ratio	1.3163	1.4972
4	Correction factor *n*	0.5001	−0.4021
5	Corrected probe rate, mm/a	1.2004	1.3046
Corrected monitoring effectiveness, %		97.36	93.83

5. Conclusions

This study addresses the insufficient monitoring effectiveness of corrosion probes in high-water-cut crude oil gathering pipelines with elevation changes. By integrating CFD local flow simulations with inclined-loop flow corrosion experiments, the influences of inlet velocity, temperature, and monitoring duration on corrosion rates and probe effectiveness were systematically examined. A multi-parameter coupled correction model was established, and field-applicable correction charts were developed. Four key conclusions were drawn, providing theoretical guidance and technical support for corrosion monitoring and protection in complex gathering pipelines with elevation changes.

1) Numerical simulations and experiments indicated that probe monitoring effectiveness was strongly influenced by inlet velocity, temperature, and monitoring duration. Effectiveness peaked at 72.88% at 0.8 m/s, then decreased to 50.10% at 1.2 m/s. Increasing the temperature reduced effectiveness from 74.63% at 20 °C to 67.00% at 60 °C. Extending the monitoring duration from 12 h to 36 h resulted in a significant improvement in effectiveness, with a relative increase of approximately 14.85 times. The critical role of monitoring duration in ensuring data stability and representativeness is emphasized.
2) A multi-parameter coupled correction model was developed, integrating flow velocity, temperature, and monitoring duration within a single predictive framework to capture the dynamic evolution of corrosion rates. Compared with conventional single-parameter methods, the model improved monitoring effectiveness predictions by over 35% on average, offering a more accurate and robust tool for dynamic corrosion assessment under complex pipeline conditions.
3) By combining CFD simulations with experimental data, a correction chart for corrosion probe monitoring effectiveness was constructed, covering flow velocities of 0.4–1.2 m/s and temperatures of 20–60 °C. The chart visualizes correction coefficients under varying operating conditions, allowing on-site personnel to rapidly adjust probe readings, substantially reducing uncertainties in corrosion assessment, while ensuring portability and practical applicability.
4) Field-scale application in a high-water-cut crude oil gathering pipeline demonstrated that the corrected probe monitoring effectiveness reached 97.36% and 93.83% in the upward- and downward-inclined segments, respectively, with an average improvement of 35.72%. These results confirm the reliability of the proposed correction model and chart under actual oilfield conditions, providing a solid basis for corrosion monitoring and integrity management, and supporting the enhancement of intrinsic operational safety.

This model is applicable only to CO_2 corrosion under conditions of water cut >92%, no H_2S, NaCl concentration of 50000 mg/L, temperature of 20–60 °C, and flow velocity of 0.4–1.2 m/s. Additional data will be collected in future work to broaden applicability, with deeper integration into the online platform. Integrate the multi-condition correction models with SCADA/DCS data channels for real-time control and anomaly handling. Establish a closed loop of online monitoring, correction, and operations and maintenance decision-making to improve long-term monitoring accuracy and management efficiency for complex undulating pipeline segments.

CRediT authorship contribution statement

Min Qin: Visualization, Formal analysis. **Xue-Ling Wu:** Writing – original draft, Methodology, Data curation. **Ke-Xi Liao:** Writing – review & editing, Funding acquisition. **Long Qin:** Validation. **Guo-Xi He:** Validation, Software. **Teng-Jiao He:** Visualization, Methodology.

Declaration of competing interest

The authors declare that they have no known competing financial interests or personal relationships that could have appeared to influence the work reported in this paper.

Acknowledgments

This work was supported by the National Natural Science Foundation of China (52174062), Sichuan Youth Fund Project (2025ZNSFSC1366) and China Postdoctoral Science Foundation (2025M772957).

References

Abdul-Majeed, G., Al-Sarkhi, A., Mohmmed, A.O., Hamoudi, M.R., 2024. An empirical approach for predicting slug to pseudo-slug transition of air/water upward two-phase flow. Exp. Comput. Multiph. Flow 6, 154–169. https://doi.org/10.1007/s42757-023-0170-1.
Al-Moubaraki, A.H., Obot, I.B., 2021. Top of the line corrosion: Causes, mechanisms, and mitigation using corrosion inhibitors. Arab. J. Chem. 14, 103116. https://doi.org/10.1016/j.arabjc.2021.103116.

Atashin, S., Toloei, A.S., Pakshir, M., 2013. Simultaneous investigation of marine factors effect on corrosion rate of SS 304 in turbulent condition. J. Mater. Eng. Perform. 22, 2038–2047. https://doi.org/10.1007/s11665-013-0473-7.

Ben Seghier, M.E.A., Höche, D., Zheludkevich, M.L., 2022. Prediction of the internal corrosion rate for oil and gas pipeline: Implementation of ensemble learning techniques. J. Nat. Gas Sci. Eng. 99, 104425. https://doi.org/10.1016/j.jngsle.2022.104425.

Cao, Y.G., Zhao, Q.K., Liu, Y.Y., 2023. Novel prediction model of tensile strain capacity for pipelines with corrosion defects. J. Pipeline Syst. Eng. Pract. 14, 04023029. https://doi.org/10.1061/JPSEA2.PSENG-1452.

Du, J., Zheng, J.Q., Liang, Y.T., et al., 2023. Deeppipe: Theory-guided prediction method based automatic machine learning for maximum pitting corrosion depth of oil and gas pipeline. Chem. Eng. Sci. 278, 118927. https://doi.org/10.1016/j.ces.2023.118927.

Fan, R.Z., Lin, M., Zheng, R.J., et al., 2025. In-situ nanoscale thickness monitoring of passive films based on electrochemical-surface plasmon resonance sensing technology. Sensor. Actuator. B Chem. 444, 138309. https://doi.org/10.1016/j.snb.2025.138309.

He, L.M., Wang, Y.H., Zhang, Q.L., et al., 2023. Electrochemical study on the macro-cell corrosion of pipeline steel partially covered by different kinds of mineral deposits. ACS Omega 8, 44013–44029. https://doi.org/10.1021/acsomega.3c06189.

He, J.Y., Xie, F., Wang, D., et al., 2024. Stress corrosion cracking behavior of buried oil and gas pipeline steel under the coexistence of magnetic field and sulfate-reducing bacteria. Pet. Sci. 21, 1320–1332. https://doi.org/10.1016/j.petsci.2023.10.013.

Hong, J.J., Wang, Z.H., Wang, C., et al., 2025. Modeling of multiphase flow with the wellbore in gas-condensate reservoirs under high gas/liquid ratio conditions and field application. SPE J. 30, 1301–1314. https://doi.org/10.2118/221053-PA.

Hu, L.H., Yi, H.L., Yang, W.J., et al., 2023. Effect of water content on corrosion behavior of X65 pipeline steel in supercritical CO_2 fluids. J. Chin. Soc. Corrosion Protect 44, 576–584. https://doi.org/10.11902/1005.4537.2023.227.

Krishnan, M.A., Prasad, N.K., Barla, N.A., 2023. High-temperature failure analysis of 25Cr35NiNb tube. Eng. Fail. Anal. 153, 107566. https://doi.org/10.1016/j.engfailanal.2023.107566.

Laleh, M., Xu, Y., Tan, M.Y.J., 2023. A three-dimensional electrode array probe designed for visualising complex and dynamically changing internal pipeline corrosion. Corros. Sci. 211, 110924. https://doi.org/10.1016/j.corsci.2022.110924.

Li, Z., Zhao, P.Q., Yang, C.H., et al., 2020. Experimental study on corrosion of multi-component thermal fluid thermal recovery well tube string. Mater. Sci. Forum 993, 1257–1264. https://doi.org/10.4028/www.scientific.net/MSF.993.1257.

Liao, K.X., Qin, M., He, G.X., et al., 2021. Study on corrosion mechanism and the risk of the shale gas gathering pipelines. Eng. Fail. Anal. 128, 105622. https://doi.org/10.1016/j.engfailanal.2021.105622.

Liu, L., Xu, Y.Z., Wang, Z.M., et al., 2021. Probing and separating corrosion and erosion of pipeline steel using electrical resistance method in conjunction with electrochemical measurements. Measurement 183, 109797. https://doi.org/10.1016/j.measurement.2021.109797.

Ma, H., Wang, Z.X., Liu, Y., et al., 2023. pH-dependent corrosion initiation behavior induced by inclusions of low alloy steel in simulated marine environments. J. Iron Steel Res. Int. 30, 2067–2079. https://doi.org/10.1007/s42243-022-00878-1.

Ma, T., Li, D.R., Zeng, L., et al., 2024. Comparative investigation on high-pressure flow accelerated corrosion at gradual contraction and gradual expansion pipes. Corros. Sci. 228, 111803. https://doi.org/10.1016/j.corsci.2023.111803.

Peng, Y.C., Chen, H., Wen, M.N., et al., 2024. Analysis of corrosion failure causes of hongjing line crude oil pipeline. J. Phys., Conf. Ser. 2821, 012020. https://doi.org/10.1088/1742-6596/2821/1/012020.

Przybyłek, M., Jeliński, T., Cysewski, P., 2019. Application of multivariate adaptive regression splines (MARSplines) for predicting Hansen solubility parameters based on 1D and 2D molecular descriptors computed from SMILES string. J. Chem. 2019, 9858371. https://doi.org/10.1155/2019/9858371.

Qin, M., Liao, K.X., Chen, S.J., et al., 2023. Numerical simulation of gas-liquid flow in inclined shale gas pipelines. Chem. Eng. Res. Des. 190, 605–618. https://doi.org/10.1016/j.cherd.2023.01.009.

Seghier, M.E.A.B., Keshtegar, B., Tee, K.F., et al., 2020. Prediction of maximum pitting corrosion depth in oil and gas pipelines. Eng. Fail. Anal. 112, 104505. https://doi.org/10.1016/j.engfailanal.2020.104505.

Shin, D.H., Hwang, H.K., Kim, H.H., et al., 2022. Evaluation of commercial corrosion sensors for real-time monitoring of pipe wall thickness under various operational conditions. Sensors 22, 7562. https://doi.org/10.3390/s22197562.

Soleymani, F., 2023. Internal corrosion monitoring of pipelines using electrochemical techniques: A comprehensive review. Protect. Met. Phys. Chem. Surface 59, 1045–1061. https://doi.org/10.1134/S207020512370096X.

Sun, M., Cui, W., Lin, N., 2023. Corrosion analysis of shale gas downhole tubing under the synergistic action of multiple factors. J. Phys., Conf. Ser. 2539, 012039. https://doi.org/10.1088/1742-6596/2539/1/012039.

Tan, X., Fan, L., Huang, Y., et al., 2021. Detection, visualization, quantification, and warning of pipe corrosion using distributed fiber optic sensors. Autom. ConStruct. 132, 103953. https://doi.org/10.1016/j.autcon.2021.103953.

Wang, W., Zhang, Y., Shuai, J., et al., 2023. Mechanical synergistic interaction between adjacent corrosion defects and its effect on pipeline failure. Pet. Sci. 20, 2452–2467. https://doi.org/10.1016/j.petsci.2023.02.026.

Wang, J., Kong, Z., Shan, J.R., et al., 2024. Corrosion rate prediction of buried oil and gas pipelines: a new deep learning method based on RF and IBWO-Optimized BiLSTM–GRU combined model. Energies 17, 5824. https://doi.org/10.3390/en17235824.

Wang, M.Y., Chen, W.B., Liang, P.N., et al., 2025. Investigation of cathodic potential induced stress corrosion cracking of marine carbon steel and its weldments in seawater. Appl. Ocean Res. 161, 104671. https://doi.org/10.1016/j.apor.2025.104671.

Wasim, M., Djukic, M.B., 2022. External corrosion of oil and gas pipelines: A review of failure mechanisms and predictive preventions. J. Nat. Gas Sci. Eng. 100, 104467. https://doi.org/10.1016/j.jngse.2022.104467.

Yang, D., Zhang, X.Y., Wang, T., et al., 2023a. Study on pipeline corrosion monitoring based on piezoelectric active time reversal method. Smart Mater. Struct. 32, 054003. https://doi.org/10.1088/1361-665X/accc1a.

Yang, D., Zhang, X.Y., Zhou, T., et al., 2023b. A novel pipeline corrosion monitoring method based on piezoelectric active sensing and CNN. Sensors 23, 855. https://doi.org/10.3390/s23020855.

Yang, S.Q., Fan, J.C., Zhao, S., et al., 2023c. Experimental study on erosion behavior of fracturing pipelines involving fluctuating stress. Wear 518–519. https://doi.org/10.1016/j.wear.2023.204626, 204626.

Yang, D., Wang, H., Wang, T., et al., 2024. Piezoelectric active sensing-based pipeline corrosion monitoring using singular spectrum analysis. Sensors 24, 4192. https://doi.org/10.3390/s24134192.

Yu, Y.T., Cheng, X.M., Wang, L., et al., 2022. Convolutional neural network-based quantitative evaluation for corrosion cracks in oil/gas pipeline by millimeter-wave imaging. IEEE Trans. Instrum. Meas. 71, 8006109. https://doi.org/10.1109/TIM.2022.3204992.

Zeng, D., Zeng, F., Peng, Z.D., et al., 2020. Fracture failure analysis of the sacrificial anode protector in a water injection well. Eng. Fail. Anal. 112, 104479. https://doi.org/10.1016/j.engfailanal.2020.104479.

Zeng, D., Dong, B.J., Zeng, F., et al., 2021. Analysis of corrosion failure and materials selection for CO_2-H_2S gas well. J. Nat. Gas Sci. Eng. 86, 103734. https://doi.org/10.1016/j.jngse.2020.103734.

Zhang, X.Q., Cheng, Q.L., Sun, W., et al., 2024. Research on a TOPSIS energy efficiency evaluation system for crude oil gathering and transportation systems based on a GA-BP neural network. Pet. Sci. 21, 621–640. https://doi.org/10.1016/j.petsci.2023.08.020.

Zhang, Q.L., Hao, L., Chen, W.B., et al., 2025. Understanding the effect of cathodic reaction on corrosion-enhanced erosion in sand-entraining electrolyte. J. Mater. Sci. Technol. 209, 103–116. https://doi.org/10.1016/j.jmst.2024.05.014.

Zhao, S., Liao, K.X., Zhou, F.L., et al., 2022. Effect of temperature on the corrosion behavior of L245NS steel in a CO_2/H_2S/O_2 multi-component thermal fluid collection and transportation system. Arabian J. Sci. Eng. 47, 11223–11237. https://doi.org/10.1007/s13369-021-05906-y.

Zhao, Y., Xi, K., Yue, P.H., et al., 2024. Impact of multi-factor coupling on the corrosion behavior of 254SMo stainless steel in an aggressive oilfield environment containing CO_2 and H_2S. Corros. Sci. 235, 112215. https://doi.org/10.1016/j.corsci.2024.112215.

Zhou, H., Ma, H.Y., Zhao, H.J., et al., 2025. Experimental study on the erosion-corrosion synergism of elbow in the case of liquid-solid swirling flow. J. Mater. Eng. Perform. 34, 968–986. https://doi.org/10.1007/s11665-023-09105-8.